Time-resolved ARPES signal in pumped semiconductors within the dynamical projective operatorial approach

Amir Eskandari-asl [1] and Adolfo Avella [1,2,3]

[1]*Dipartimento di Fisica "E.R. Caianiello", Università degli Studi di Salerno, I-84084 Fisciano (SA), Italy*

[2]*CNR-SPIN, Unità di Salerno, I-84084 Fisciano (SA), Italy*

[3]*CNISM, Unità di Salerno, Università degli Studi di Salerno, I-84084 Fisciano (SA), Italy*

(Received 25 April 2024; revised 16 July 2024; accepted 19 August 2024; published 16 September 2024)

In this manuscript, after discussing in detail the internals of our recently developed method, the dynamical projective operatorial approach (DPOA), we provide the framework to apply this method to pumped semiconductor lattice systems and, in particular, to study and analyze their electronic excitations and TR-ARPES signal. The expressions for relevant out-of-equilibrium Green's functions and TR-ARPES signal are given within the DPOA framework and, defining a retarded TR-ARPES signal, it is shown that it is possible to obtain an out-of-equilibrium version of the fluctuation-dissipation theorem. We clarify how single- and multiphoton resonances, rigid shifts, band dressings, and different types of sidebands emerge in the TR-ARPES signal. We also propose protocols for evaluating the strength of single- and multiphoton resonances and for assigning the residual excited electronic population at each crystal momentum and band to a specific excitation process. Hamiltonians, where intra- and interband transitions are selectively inhibited, are defined and used to analyze the effects on the TR-ARPES signal and the residual electronic excited population. Three relevant cases of light-matter coupling are examined within the dipole gauge: only a local dipole, only the Peierls substitution in the hopping term, and both terms at once. The transient and residual pump effects are studied in detail, including the consequences of the lattice symmetries at different crystal momenta on the TR-ARPES signal. A detailed study of the dependence of the TR-ARPES signal on the probe-pulse characteristics is also reported. To provide a guideline for understanding the complex effects and interplays and the variety of possible physical phenomena without being limited by the characteristics of a single particular *real* material, we have chosen to study a prototypical pumped two-band semiconductor lattice system.

DOI: 10.1103/PhysRevB.110.094309

I. INTRODUCTION

The modern developments in technology made it possible to study condensed matter systems in the attosecond regime and investigate their real-time dynamics upon perturbation by ultrashort and intense electromagnetic pulses, the so called pump-probe setups [1–6]. Investigating the real-time behavior of electronic excitations induced by the laser pulse reveals the fundamental processes that govern the physics of the system under study [7–11]. One avenue is to investigate the response of the solid by reading out the high-harmonic generation upon irradiation [12–21]. In other pump-probe setups, the system is pumped with an intense laser pulse, usually in the IR regime and with a duration ranging from few to hundreds of fs, and analyzed using a positively or negatively delayed probe pulse by measuring either the transient change in the optical properties [7,8,18,22–32] or the time-resolved angle-resolved photoemission spectroscopy (TR-ARPES) signal [11,33–40]. Even though the theoretical method we introduce in this manuscript is in principle capable of dealing with any time-dependent system response, as optical properties [41], in this paper, we will mainly focus on its description of the TR-ARPES signal.

ARPES investigates the electronic band structure of materials by analyzing the energy and momentum distribution of the electrons ejected from a solid via photoelectric effect [42–48]. Instead, in pump-probe setups, TR-ARPES is exploited to determine the out-of-equilibrium electronic properties of materials by measuring the signal as a function of the time delay between the pump and probe pulses [48–52]. TR-ARPES measurements in pump-probe setups can reveal the different dynamical processes taking place in the system [48], which are of fundamental importance for understanding the underlying physics and eventually engineering materials for practical purposes. Thanks to the capability of monitoring the dynamics of the electronic excitations, TR-ARPES can give valuable information about the bands above the Fermi energy, well beyond what one can achieve by measuring thermal excitations at equilibrium [53–55]. Moreover, TR-ARPES can measure and study the dressing of the main bands and the emergence of sidebands due to the pump pulse [37,56], opening a pathway to novel applications in ultrafast engineering of materials. TR-ARPES measurements can be used to investigate many other complex effects induced by the pump pulse such as the perturbation (melting, switching, emergence, etc.) of ordered states in materials [11,33,34] and the dynamical excitation of collective modes [36,57,58], just to give a few examples.

To understand the underlying physical phenomena and microscopic processes induced by the pumping of materials,

such advanced experimental studies require their theoretical description and numerical simulation. The standard approach to the numerical study of the out-of-equilibrium behavior of a material pumped with an intense laser pulse is the time-dependent density functional theory (TD-DFT) [27,32,59–65], which is unfortunately rather time-consuming and computationally expensive [66]. Moreover, it is not easy to get deep insights into the underlying physics through TD-DFT simulations just using (without *tampering*) currently available software packages, while, in a model-Hamiltonian approach, it is possible to switch on and off terms and investigate their relative relevance and interplay [66].

Model-Hamiltonian approaches, for both matter and light-matter interaction terms, rely on parameters supplied by DFT calculations at equilibrium for *real* materials [67]. If the material is strongly correlated, one can use the dynamical mean-field theory to compute its out-of-equilibrium properties if the number of degrees of freedom involved (spin, bands, atoms in the basis, etc.) is limited [6,68–70]. However, for weakly correlated materials, such as most of the semiconductors, the Hamiltonian can be mapped to an effective quadratic form, for which one can in principle compute the time-dependent single-particle density-matrix and/or higher-order correlation functions according to the probing scheme [56,71]. Another approach that is suitable for effective few-band models is the so called Houston method in which one expands electronic single-particle wave functions in terms of the instantaneous eigenstates of the time-dependent Hamiltonian and solves the equations of motion for the expansion coefficients within some approximations [27,72]. The relevance of Houston method is to provide a framework to disentangle the effects of different processes, in particular those related to the interband and to the intraband transitions, and their interplay.

At any rate, model-Hamiltonian approaches cannot be applied so easily to *real* materials as one either run the risk to use oversimplified models that could lose some important features or has to find an efficient way to deal with the actual very complicated Hamiltonians describing many degrees of freedom at once [66]. Even for quadratic Hamiltonians, one needs to numerically solve the equations of motion of the multiparticle density matrices or multitime correlation functions, which are needed to describe response functions, such as the optical conductivity, or for computing the TR-ARPES signal. Unfortunately, without a proper framework, such calculations can be computationally quite heavy and eventually unaffordable. Recently, we designed and developed a novel method, the dynamical projective operatorial approach (DPOA), and used it to analyze the transient and residual electronic photoexcitations in ultrafast (attosecond) pumped germanium [30,31]. We benchmarked our results with those obtained through TD-DFT calculations, which were in turn validated by direct comparison to the experimental results for the differential transient reflectivity. Moreover, DPOA allowed us to use much finer momentum grids than the ones affordable by TD-DFT, and unravel the actual relevant pumping processes, as well as the individual roles of different mechanisms and their interplay.

DPOA is a quite versatile model-Hamiltonian approach that deals with the time evolution of composite operators [73–78] and is capable of simulating *real* materials, and the time-dependent transitions among their actual numerous bands [30,31]. DPOA is, in principle, capable of tackling strongly correlated systems as well [79]. In this paper, we delve into DPOA by reporting its detailed derivation and its quadratic-Hamiltonian version, which is particularly fast and efficient. Such a version is very useful for semiconductors where one can usually safely discard the *dynamical* Coloumb interaction. We also report how to compute all single- and multiparticle single- and multitime observables and correlation functions within this approach. Moreover, we provide an efficient way to implement the Peierls substitution through a numerically exact expansion and to compute the mth partial derivative in momentum space of the hopping and of the dipole terms appearing in such expansion. This allows to analyze and characterize the terms in such an expansion defining the related characteristic frequencies, timescales, bandwidths, and relative phases that explain the emergence and the features of different kinds of sidebands (multiphoton resonant, non resonant, envelope,...) considering also the effects of the finite width of the envelope of the pump pulse. The presence of the envelope modifies and generalizes also the Rabi-like phenomenology that takes place when some of the band gaps are in resonance with integer multiples of the central frequency of the pump pulse. Such single- and multiphoton resonances determine the accumulation of (residual) electronic excited populations after the pump pulse turns off. Then, we propose a procedure to determine the strength of a multiphoton *nonexact* resonance and through this to assign residual electronic excited populations per momentum and band to specific single- and multiphoton resonant processes. Furthermore, we use our approach to reproduce the Houston method, generalize it to second quantization, and to obtain numerically exact expectation values of the Houston coefficients overcoming its limitations and drawbacks. We also show that the separation of interband and intraband transition effects can be obtained in DPOA without any ambiguity, while such separation is questionable within the Houston approach. Moreover, we show how to compute Green's functions (GFs) using DPOA, and hence the TR-ARPES signal. As the standard spectral functions can become negative out of equilibrium, there is no out-of-equilibrium counter-part of the fluctuation-dissipation theorem [70]. Indeed, by defining the retarded TR-ARPES signal, we generalize the fluctuation-dissipation theorem and find its equivalent out of equilibrium for TR-ARPES signal, which can be useful to better understand and compute the out-of-equilibrium energy bands of pumped systems.

As already mentioned above, very recently, we exploited DPOA to unveil the various charge-injection mechanisms active in germanium [30,31]. In this work, to analyze and discuss a larger variety of fundamental physical processes without the limitations imposed by the peculiarities of a specific *real* material, we apply DPOA to a nontrivial toy model. We analyze a two-band (valence-conduction) model and consider three relevant cases by switching on and off the Peierls substitution in the hopping term (relevant to bulk systems) and a local dipole term (relevant to systems such as quantum dots and molecules and low-dimensional systems with transverse pumps). We discuss the main effects of the two terms separately as well as the relevance of their interplay. In particular,

we analyze how the first-order (in the pumping field) terms of the two types of light-matter couplings assist the higher-order ones and how their decomposition in terms of intra- and interband components can help understanding the actual phenomenology. We compute and analyze, in connection to the symmetries of the system, the lesser and the retarded TR-ARPES signals as well as the residual excited population. We discuss the broadening of the out-of-equilibrium TR-ARPES bands and their relationship to the equilibrium bands (the rigid shift due to the even terms starting from the inverse-mass one) and the instantaneous eigenstates. Moreover, we discuss the suppression of the different kinds of sidebands and, in particular, of the resonant ones in connection to the vanishing of velocity (one-photon sideband) and inverse-mass (two-photon sideband) terms due to band symmetries and how such *symmetry protection* is lost in the presence of the dipole term. We also introduce another type of side bands induced by the envelope and even-terms. Additionally, we investigate the accumulation of residual electronic excited population (clearly visible also in the lesser TR-ARPES signal) induced by Rabi-like oscillations at single- and multiphoton resonant *non-symmetry-protected* $\mathbf{k}$ points and the characteristics of such oscillations in terms of the pump-pulse features. The effects of inhibiting selectively intra- and interband transitions are also studied on the TR-ARPES signal and on the residual electronic excited population. Moreover, we study the changes in the characteristics of TR-ARPES signal on varying the pump-probe delay and the width of the probe pulse.

In addition, we report a detailed derivation of the dipole-gauge second-quantization Hamiltonian for light-matter interaction from the velocity-gauge first-quantization one within the minimal coupling. The expressions of Hamiltonian, electronic current, and charge density operators are derived requesting charge conservation and cast in real and momentum space and in Bloch and Wannier basis. Such expressions are fundamental for the current study (residual excited electronic population and TR-ARPES signal) and for the determination of optical response functions.

The manuscript is organized as follow. In Sec. II, we introduce DPOA and its quadratic-Hamiltonian version for a pumped lattice system within the dipole gauge as well as its relation to the single-particle density-matrix and Houston approaches, and discuss in detail how to analyze different phenomena and their emergent effects. Moreover, we provide the formulation to obtain the out-of-equilibrium Green's function of a system within DPOA as well as the TR-ARPES signal and an out-of-equilibrium version of the fluctuation-dissipation theorem. In Sec. III, to show how DPOA works in a fundamental and prototypical case, we present and discuss in detail the DPOA results for the TR-ARPES signal and the residual electronic excited population of a pumped two-band (valence-conduction) system considering different cases of the case of light-matter interaction, and conclude with a study of the TR-ARPES signal dependence on the probe-pulse characteristics. Sec. IV, summarizes this work and gives an outlook. Finally, we included four appendices regarding the derivation of the velocity and the dipole gauges in second quantization (Appendix A), the effects of the oscillations of the diagonal elements on the multiphoton resonances (Appendix B), the Houston approach in first quantization (Appendix C) and the out-of-equilibrium spectral functions (Appendix D).

II. THEORY

A. Dynamical projective operatorial approach (DPOA)

For any system at equilibrium, described by a general time-independent Hamiltonian $\mathcal{H}$ in second quantization and Heisenberg picture, one can find as many sets of *composite* operators $\mathcal{C}_\alpha^\dagger = (\mathcal{C}_{\alpha,1}^\dagger, \ldots, \mathcal{C}_{\alpha,a}^\dagger, \ldots)$, as many degrees of freedom characterizing the system (spin, orbital, momentum, etc.), which close their hierarchy of the equations of motion [73–78]. A very effective measure of the degree of correlation in the system is the ratio between the number of independent (disjoint) sets and the number of degrees of freedom: for a noncorrelated system this ratio is 1, and it tends to 0 (1) according to how much the system is strongly (weakly) correlated.

To study the properties of a solid-state system and its linear response, two types of sets are essential. One is the set stemming from the canonical electronic (fermionic) operators of the system under study, $c_\nu(\mathbf{r}, t)$, where, for instance, $\mathbf{r}$ can be the site in a Bravais lattice and ν collects all possible degrees of freedom (spin, orbital, atom in a basis, etc.). The other is the set stemming from the canonical charge, spin, orbital,... number and ladder (bosoniclike) operators of the system under study that allow to obtain the related susceptibilities.

Now, let us consider a general time-dependent external perturbation applied to the system: $\mathcal{H} \to \mathcal{H}(t)$. For instance, it can be an electromagnetic pump pulse whose interaction with the system is usually described via the minimal coupling. Such a perturbation preserves the *closure* of the hierarchy of the equations of motion of $\mathcal{C}_\alpha$ as it usually changes only the single-particle term of the Hamiltonian [67]; therefore,

$$i\hbar\partial_t \mathcal{C}_\alpha(t) = [\mathcal{C}_\alpha(t), \mathcal{H}(t)] = \Xi_\alpha(t) \odot \mathcal{C}_\alpha(t), \tag{1}$$

where $\odot$ is the matrix product in the space of the operators in a specific set α, while $\Xi_\alpha(t)$ and $\mathcal{C}_{\alpha,a}(t)$ are the time-dependent energy matrix and eigenoperators in the Heisenberg picture, respectively. These considerations guided us to design and devise the dynamical projective operatorial approach (DPOA) according to which we have

$$\mathcal{C}_\alpha(t) = P_\alpha(t, t_0) \odot \mathcal{C}_\alpha(t_0) \quad \forall t \geqslant t_0, \tag{2}$$

where $P_\alpha(t, t_0)$ are called dynamical projection matrices. Equation (2) can be verified using mathematical induction as follows. Basis: At time $t = t_0$, Eq. (2) obviously holds with $P_\alpha(t_0, t_0) = \mathbf{1}$. Induction step: Let us discretize the time axis in terms of an infinitesimal time step $\Delta t \to 0$ ($t_n = n\,\Delta t + t_0$) and let us assume that Eq. (2) holds for time t_n, i.e.,

$$\mathcal{C}_\alpha(t_n) = P_\alpha(t_n, t_0) \odot \mathcal{C}_\alpha(t_0), \tag{3}$$

Then, for time $t_{n+1} = t_n + \Delta t$, we have

$$\begin{aligned}\mathcal{C}_\alpha(t_{n+1}) &= \mathcal{C}_\alpha(t_n) + \Delta t\,\partial_t \mathcal{C}_\alpha(t_n) \\ &= \left[P_\alpha(t_n, t_0) - \Delta t \frac{i}{\hbar}\Xi_\alpha(t_n) \odot P_\alpha(t_n, t_0)\right] \odot \mathcal{C}_\alpha(t_0),\end{aligned} \tag{4}$$

that closes the proof and suggests the following relation:

$$P_\alpha(t_{n+1}, t_0) = P_\alpha(t_n, t_0) - \Delta t \frac{i}{\hbar}\Xi_\alpha(t_n) \odot P_\alpha(t_n, t_0). \tag{5}$$

In the following, we choose as initial time t_0 any time before the application of the pump pulse (e.g., $t_0 \to -\infty$) and, for the sake of simplicity, we indicate the dynamical projection matrices using just one time argument $P_\alpha(t, t_0) \to P_\alpha(t)$. Then, $\mathcal{C}_\alpha(t_0)$ simply stands for the operatorial basis describing the system at equilibrium.

Applying the limit $\Delta t \to 0$ to Eq. (5), one obtains the equation of motion for the dynamical projection matrix as

$$i\hbar\partial_t P_\alpha(t) = \Xi_\alpha(t) \odot P_\alpha(t), \tag{6}$$

with initial condition $P_\alpha(t_0) = \mathbf{1}$. For stationary Hamiltonians, i.e., when $\Xi_\alpha(t) \to \Xi_\alpha^{(0)}$, the solution of Eq. (6) is simply $P_\alpha^{(0)}(t) = e^{-\frac{i}{\hbar}(t-t_0)\Xi_\alpha^{(0)}}$. However, for a general perturbed system, where $\Xi_\alpha(t) = \Xi_\alpha^{(0)} + \Xi_\alpha^{(1)}(t)$, one needs to numerically compute the dynamical projection matrix $P_\alpha(t)$ from which it is possible to obtain all out-of-equilibrium properties and response functions of the system.

Finally, it is worth noting that rewriting $P_\alpha(t) = P_\alpha^{(0)}(t) \odot P_\alpha^{\text{int}}(t) = e^{-\frac{i}{\hbar}(t-t_0)\Xi_\alpha^{(0)}} \odot P_\alpha^{\text{int}}(t)$, we can deduce the following reduced equation of motion

$$i\hbar\partial_t P_\alpha^{\text{int}}(t) = \Xi_\alpha^{(1)\text{int}}(t) \odot P_\alpha^{\text{int}}(t), \tag{7}$$

where $\Xi_\alpha^{(1)\text{int}}(t) = e^{\frac{i}{\hbar}(t-t_0)\Xi_\alpha^{(0)}} \odot \Xi_\alpha^{(1)}(t) \odot e^{-\frac{i}{\hbar}(t-t_0)\Xi_\alpha^{(0)}}$. Equation (7) can be helpful (i) to stabilize the numerical solution when high frequencies are involved and (ii) to apply any approximation only to the time-dependent component of the Hamiltonian and preserve intact the equilibrium dynamics. The equivalent (iterative) integro-differential equation reads as

$$P_\alpha^{\text{int}}(t) = \mathbf{1} - \frac{i}{\hbar}\int_{t_0}^{t} dt_1\, \Xi_\alpha^{(1)\text{int}}(t_1) \odot P_\alpha^{\text{int}}(t_1). \tag{8}$$

B. Quadratic Hamiltonians

Quadratic Hamiltonians play a fundamental role in many fields of physics as they retain the full complexity of a system in terms of its degrees of freedom as well as the possibility to describe to full extent the effects of applying a (time-dependent) external field or gradient to the system. Obviously, one cannot describe strong correlations, that is a deep and intense interplay between degrees of freedom, but this is not essential in many cases.

As it specifically regards solid-state systems, the most relevant quadratic Hamiltonians are the tight-binding ones that can be built for *real* materials through wannierization (for example, by exploiting Wannier90 code [80]) of the basic standard results of almost any DFT code available. This procedure preserves the *static* Coloumb interaction among the electrons (appearing in the exchange integral within DFT), which usually results in the opening of gaps and in band repulsion. In presence of a time-dependent perturbation, e.g., a pump pulse, TD-DFT is usually applied although it results in very lengthy and very resource-consuming calculations. DPOA for time-dependent quadratic Hamiltonians is instead very fast and efficient although it neglects the *dynamical* Coloumb interaction, which can be safely discarded in many cases. Even excitonic effects can be easily described in DPOA by choosing the proper effective terms in the Hamiltonian under analysis and working with effective excitonic creation and annihilation operators. It is worth noticing that DPOA allows to retain and to catch the physics of all time-dependent *complications* and all transitions among the actual, although very numerous, bands of *real* materials [30].

Let us consider a system described by the following completely general time-dependent quadratic Hamiltonian in second quantization and Heisenberg picture

$$\mathcal{H}(t) = a^\dagger(t) \odot \Xi(t) \odot a(t), \tag{9}$$

where $a^\dagger(t) = (a_1^\dagger(t), \ldots, a_n^\dagger(t), \ldots)$ is the creation operator of a general quasiparticle (either fermionic or bosonic including free electrons, electrons in lattice, electrons in molecules, phonons, magnons, photons, excitons, plasmons, polarons, polaritons, etc.) in Heisenberg picture and we use a vectorial notation with respect to the set of quantum numbers $n = (n_1, n_2, \ldots)$ that label all degrees of freedom of the system under analysis. $\Xi(t) = \Xi^{(0)} + \Xi^{(1)}(t)$ is the energy matrix in which $\Xi^{(0)}$ gives the equilibrium Hamiltonian, $\mathcal{H}^{(0)}$, and matrix $\Xi^{(1)}(t)$ describes the coupling of the system to the time-dependent external pump pulse and gives $\mathcal{H}^{(1)}(t)$. As the main simplification comes from the Hamiltonian being quadratic, the eigenoperators of the system are just the $a_n(t)$, and according to the general theory discussed above, we have

$$a(t) = P(t) \odot a(t_0), \tag{10}$$

$$i\hbar\partial_t P(t) = \Xi(t) \odot P(t), \tag{11}$$

with the initial condition $P(t_0) = \mathbf{1}$. At each instant of time, the canonical commutation relations obeyed by $a_n(t)$ lead to $P(t) \odot P^\dagger(t) = \mathbf{1}$, which is a useful relation to check the stability and the precision over time of any numerical approach used to compute $P(t)$.

C. Single-particle density matrix (SPDM)

To show how to obtain the dynamical properties of the system using the dynamical projection matrices $P(t)$, we consider first the single-particle density matrix (SPDM) $\rho(t) = \langle a(t) \otimes a^\dagger(t)\rangle$, whose equation of motion reads as

$$i\hbar\partial_t \rho(t) = [\Xi(t), \rho(t)]. \tag{12}$$

Once the time evolution of $\rho(t)$ is known, it is possible to compute the average of any single-particle single-time operator $X(t) = a^\dagger(t) \odot \mathcal{X}(t) \odot a(t)$ and, therefore, of the corresponding physical quantity as follows:

$$\langle X(t)\rangle = \text{Tr}(\mathcal{X}(t) \odot [\mathbf{1} - \rho(t)]). \tag{13}$$

Given that $\rho(t) = P(t) \odot \langle a(t_0) \otimes a^\dagger(t_0)\rangle \odot P^\dagger(t) = P(t) \odot \rho(t_0) \odot P^\dagger(t)$, we have

$$\langle X(t)\rangle = \text{Tr}[P^\dagger(t) \odot \mathcal{X}(t) \odot P(t) \odot [\mathbf{1} - \rho(t_0)]]. \tag{14}$$

If we choose the quantum numbers n such that the corresponding operators diagonalize the equilibrium Hamiltonian $H^{(0)}$, that is $\Xi_{nm}^{(0)} = \delta_{nm}\varepsilon_n$, we simply have $\rho_{nm}(t_0) = \delta_{nm}(1 - \eta f_\eta(\varepsilon_n))$ where $\eta = \pm 1$ correspond to fermionic (bosonic) system and $f_\eta(\varepsilon) = \frac{1}{e^{\beta\varepsilon}+\eta}$ is the related equilibrium distribution function. Once the dynamical projection matrices $P(t)$ are known at all times, it is possible to recover all the results of the SPDM approach, and more importantly, go beyond them.

Indeed, we are not limited to single-particle properties and even within these latter not to single-time ones. For instance, given a general single-particle two-time operator $Y(t,t') = a^\dagger(t) \odot \mathcal{Y}(t,t') \odot a(t')$, the time evolution of its average $\langle Y(t,t')\rangle$ is simply given by

$$\langle Y(t,t')\rangle = \mathrm{Tr}[P^\dagger(t) \odot \mathcal{Y}(t,t') \odot P(t') \odot [\mathbf{1} - \rho(t_0)]]. \tag{15}$$

The extension to multiparticle multitime operators is straightforward and requires only the knowledge of equilibrium averages, which for quadratic Hamiltonians can be easily calculated thanks to the Wick's theorem.

D. Pumped lattice systems, Peierls expansion, and multiphoton resonances

Let us consider an electromagnetic pump pulse applied to a lattice system after time t_0, and described by the vector potential $\boldsymbol{A}(t)$ and the electric field $\boldsymbol{E}(t) = -\partial_t \boldsymbol{A}(t)$ in the Coulomb gauge. Accordingly, in the dipole gauge, the dynamics is governed by the Hamiltonian $\mathcal{H}(t) = \sum_{\mathbf{k},\nu,\nu'} \tilde{c}^\dagger_{\mathbf{k},\nu}(t)\tilde{\Xi}_{\mathbf{k},\nu,\nu'}(t)\tilde{c}_{\mathbf{k},\nu'}(t)$, where $\tilde{c}_{\mathbf{k},\nu}(t)$ is the annihilation operator of an electron with momentum $\mathbf{k}$ (in the first Brillouin zone) in the localized state ν (e.g., a maximally localized Wannier state) and [67] (see Appendix A for derivation)

$$\tilde{\Xi}_{\mathbf{k},\nu,\nu'}(t) = \tilde{T}_{\mathbf{k}+\frac{e}{\hbar}\boldsymbol{A}(t),\nu,\nu'} + e\boldsymbol{E}(t) \bullet \tilde{\boldsymbol{D}}_{\mathbf{k}+\frac{e}{\hbar}\boldsymbol{A}(t),\nu,\nu'}. \tag{16}$$

$\tilde{T}_{\mathbf{k},\nu,\nu'}$ and $\tilde{\boldsymbol{D}}_{\mathbf{k},\nu,\nu'}$ are the hopping and dipole matrix elements in the reciprocal space, respectively, and the over-script $\sim$ indicates that they are expressed in the basis of the localized states, $e > 0$ is the value of electronic charge, and $\bullet$ is the scalar product between two vectors in the Cartesian space. The momentum shift by the vector potential, $\mathbf{k} + \frac{e}{\hbar}\boldsymbol{A}(t)$, resembles the Peierls substitution [81,82] and Eq. (16) can be considered as its generalization to multiband systems [67]. Equation (16) shows that the coupling to the pump pulse is two fold: the Peierls substitution (in both $\tilde{T}_{\mathbf{k},\nu,\nu'}$ and $\tilde{\boldsymbol{D}}_{\mathbf{k},\nu,\nu'}$) and the dipole term $\boldsymbol{E}(t) \bullet \boldsymbol{D}$. It is worth noting that, for $(d < 3)$-dimensional systems with transverse pump-pulse polarization there is no coupling through the Peierls substitution and the dipole term is the only coupling to the external field.

The equilibrium Hamiltonian reduces to $\tilde{\Xi}_{\mathbf{k},\nu,\nu'}(t \leqslant t_0) = \tilde{T}_{\mathbf{k},\nu,\nu'}$, which can be diagonalized through the matrix $\Omega_{\mathbf{k},\nu,n}$ as follows:

$$\delta_{n,n'}\varepsilon_{\mathbf{k},n} = \sum_{\nu,\nu'} \Omega^\dagger_{\mathbf{k},n,\nu}\tilde{T}_{\mathbf{k},\nu,\nu'}\Omega_{\mathbf{k},\nu',n'}, \tag{17}$$

where n indicates the energy band. Being diagonal at equilibrium, the band basis provides a great advantage in computations. The transformation to the band basis is performed as

$$\boldsymbol{D}_{\mathbf{k},n,n'} = \sum_{\nu,\nu'} \Omega^\dagger_{\mathbf{k},n,\nu}\tilde{\boldsymbol{D}}_{\mathbf{k},\nu,\nu'}\Omega_{\mathbf{k},\nu',n'}, \tag{18}$$

$$\Xi_{\mathbf{k},n,n'}(t) = \sum_{\nu,\nu'} \Omega^\dagger_{\mathbf{k},n,\nu}\tilde{\Xi}_{\mathbf{k},\nu,\nu'}(t)\Omega_{\mathbf{k},\nu',n'}, \tag{19}$$

and

$$c_{\mathbf{k},n}(t) = \sum_{\nu} \Omega^\dagger_{\mathbf{k},n,\nu}\tilde{c}_{\mathbf{k},\nu}(t). \tag{20}$$

It is worth recalling that $c_{\mathbf{k}}(t) = P_{\mathbf{k}}(t) \odot c_{\mathbf{k}}(t_0)$, where $P_{\mathbf{k}}(t_0) = \mathbf{1}$ and $i\hbar\partial_t P_{\mathbf{k}}(t) = \Xi_{\mathbf{k}}(t) \odot P_{\mathbf{k}}(t)$. Moreover, $N_{\mathbf{k},n}(t) = \langle c^\dagger_{\mathbf{k},n}(t)c_{\mathbf{k},n}(t)\rangle$, the time-dependent number of electrons in band n with momentum $\mathbf{k}$, is given by

$$N_{\mathbf{k},n}(t) = \sum_{n'} P_{\mathbf{k},n,n'}(t) f_+(\varepsilon_{\mathbf{k},n'}) P^\dagger_{\mathbf{k},n',n}(t). \tag{21}$$

For *real* materials (our recent work on germanium being an example [30]), with many bands involved in the dynamics and hopping and dipole parameters obtained in real space through wannerization, the presence of the Peierls substitution, $\mathbf{k} + \frac{e}{\hbar}\boldsymbol{A}(t)$, in Eq. (16) makes any time-dependent measure extremely time-consuming, as it is necessary, at each time step in the numerical time grid, to Fourier transform again and again, because of the shift, the hopping and dipole matrices to momentum space on the numerical momentum grid and, finally, perform the rotation to the band space. A very efficient way to deal with this problem, which makes it possible to study systems with many bands without overheads in terms of time consumption and numerical precision, exploits the expansion of the hopping matrix and of the dipole matrix with respect to the vector potential, to sufficiently high order (determined by the maximum strength of the vector potential and the bandwidth of the system) and uses the expansion coefficients, computed once for all, at all times:

$$T_{\mathbf{k}+\frac{e}{\hbar}\boldsymbol{A}(t)}(t) = \sum_{m=0}^{\infty} \frac{1}{m!}\Omega^\dagger_{\mathbf{k}} \odot \left[\partial^{(m)}_{k_A}\tilde{T}_{\mathbf{k}}\right] \odot \Omega_{\mathbf{k}}\left(\frac{e}{\hbar}A(t)\right)^m, \tag{22}$$

$$\boldsymbol{D}_{\mathbf{k}+\frac{e}{\hbar}\boldsymbol{A}(t)} = \sum_{m=0}^{\infty} \frac{1}{m!}\Omega^\dagger_{\mathbf{k}} \odot \left[\partial^{(m)}_{k_A}\tilde{\boldsymbol{D}}_{\mathbf{k}}\right] \odot \Omega_{\mathbf{k}}\left(\frac{e}{\hbar}A(t)\right)^m, \tag{23}$$

where $\partial^{(m)}_{k_A}$ is the mth partial derivative in momentum space in the direction of the pump-pulse polarization, $\hat{A}$, and $A(t)$ is the magnitude of the vector potential: $\boldsymbol{A}(t) = A(t)\hat{A}$. We call this procedure *Peierls expansion* hereafter. It is noteworthy that $T_{\mathbf{k}}$ and $\boldsymbol{D}_{\mathbf{k}}$ are, by construction, analytic functions of the momentum $\mathbf{k}$ [see Eqs. (A49) and (A50)], and, therefore, the *Peierls expansion* always converges. The expansion coefficients, that is, the mth partial derivatives, tend to zero by increasing m since the hopping and dipole matrices in direct space are not infinitely long range thanks to the localization of the Wannier states. These coefficients can be efficiently computed by means of the Fourier transformation as

$$\partial^{(m)}_{k_A}\tilde{T}_{\mathbf{k}} = \sum_{\mathbf{i}} (-i\hat{A} \bullet \mathbf{R}_{\mathbf{i}})^m e^{-i\mathbf{k}\bullet\mathbf{R}_{\mathbf{i}}}\tilde{T}_{\mathbf{R}_{\mathbf{i}}}, \tag{24}$$

$$\partial^{(m)}_{k_A}\tilde{\boldsymbol{D}}_{\mathbf{k}} = \sum_{\mathbf{i}} (-i\hat{A} \bullet \mathbf{R}_{\mathbf{i}})^m e^{-i\mathbf{k}\bullet\mathbf{R}_{\mathbf{i}}}\tilde{\boldsymbol{D}}_{\mathbf{R}_{\mathbf{i}}}, \tag{25}$$

where $\tilde{T}_{\mathbf{R}_{\mathbf{i}}}$ and $\tilde{\boldsymbol{D}}_{\mathbf{R}_{\mathbf{i}}}$ are the hopping and dipole matrices, respectively, in the direct space, as outputted, for example, by the wannierization procedure. Another important point to mention is that even for very high intensities of the pump pulse, $\frac{e}{\hbar}A(t)$ is at maximum just a few percent of the extension of the Brillouin zone in *real* materials [30]. This fixes an upper bound for the maximum value of m to be actually used in the numerical evaluation of the *Peierls expansions*.

Such an expansion, even if not used in the actual numerical calculations, is of fundamental relevance as it gives insight

into the actual excitation processes active in the system and connects them to the symmetries of the band structure and of the dipole couplings. According to a well-established practice, we call the coefficient of the first-order (second-order) term of the *Peierls expansion*, Eq. (22), of the hopping term T as the velocity (inverse-mass) term.

The pump pulse $A(t)$ can be usually represented as $A(t) = A_0 S(t)\cos(\omega_{\rm pu} t + \phi)$ where $\omega_{\rm pu}$ is the central frequency of the pulse, ϕ is its phase, and $S(t)$ is an envelope function that vanishes at $t \to \pm\infty$. A usual expression for the envelope function is a Gaussian, $S(t) = e^{-4\ln 2 t^2/\tau_{\rm pu}^2}$, where $\tau_{\rm pu}$ is its full-width at half maximum (FWHM) and, for the sake of simplicity, its center is just at $t = 0$. Such an envelope gives a finite bandwidth to the pulse of the order $2\pi\hbar\tau_{\rm pu}^{-1}$, where $\tau_{\rm pu}^{-1}$ is FWHM of the corresponding Gaussian in frequency domain.

Given the above expression for the pump pulse, $A(t)$, we can expand its mth power, $A^m(t)$, and get

$$\Lambda_{\mathbf{k}+\frac{e}{\hbar}\boldsymbol{A}(t)}(t) = \Omega_{\mathbf{k}}^{\dagger} \odot \tilde{\Lambda}_{\mathbf{k}} \odot \Omega_{\mathbf{k}} + \sum_{m=1}^{\infty} \Theta_{0,m}(t) + 2\sum_{l=1}^{\infty}\left[\sum_{m=0}^{\infty}\Theta_{l,m}(t)\right]\cos(l\omega_{\rm pu}t + l\phi), \quad (26)$$

$$\Theta_{l,m}(t) = \frac{\left(\frac{eA_0S(t)}{2\hbar}\right)^{2m+l}}{m!(m+l)!}\Omega_{\mathbf{k}}^{\dagger} \odot \left[\partial_{k_A}^{(2m+l)}\tilde{\Lambda}_{\mathbf{k}}\right] \odot \Omega_{\mathbf{k}}, \quad (27)$$

where Λ can be either the hopping matrix T or the dipole matrix D. Such an expression allows us to understand the excitation processes. The first term on the right-hand side is just the pristine (time-independent) hopping or dipole matrix. The second term would result in a $\mathbf{k}$-dependent energy shift coming from the even derivatives (mainly from the inverse-mass coefficient of the hopping term) if there would be no envelope function $S(t)$. Actually, it is time-dependent because of the envelope function $S(t)$, but not periodic, and will lead to the emergence of nonresonant side bands, as we will show in Sec. III, on a timescale of the order $\frac{\tau_{\rm pu}}{\sqrt{2}}$ around the envelope center provided that the energy-band symmetries do not require the inverse-mass term (and higher-order even terms) to be zero. The third term leads to Rabi-like l-photon resonances whenever the energy gap between any two bands in the system, not both empty or full at a certain instant of time, is close to $l\hbar\omega_{\rm pu}$ within a bandwidth of order $2\pi\hbar\sqrt{l}\tau_{\rm pu}^{-1}$. In realistic pump-probe setups, given the bandwidths of the valence and conduction portion of the band structure involved in the dynamical processes, usually the maximum number of relevant l (i.e., the maximum relevant number of photon processes) is low, which is connected to the fact that only the first few terms of the *Peierls expansions* are needed in actual numerical calculations, as discussed above. Each l-component of this term is active on a timescale of the order $\frac{\tau_{\rm pu}}{\sqrt{l}}$ around the envelope center and has a phase shift of $(l-1)\phi$ with respect to the $l = 1$ component. For very short values of $\tau_{\rm pu}$ with respect to $2\pi\omega_{\rm pu}^{-1}$, that is, when we have so few cycles of the pump pulse within the envelope to hardly recognize any oscillation, we end up in an impulsive regime. Actually, given that the oscillation period decreases with l^{-1} while the FWHM decreases with $l^{-\frac{1}{2}}$, even in the case where lower-l terms are impulsive, sufficiently higher-l terms are anyway oscillatory, although these latter can have a negligible effect on the dynamics.

Consequently, in lattice systems, one origin of multiphoton resonances are the nonlinear terms in the Peierls expansion. Another origin is the oscillatory behavior of the diagonal terms of the coupling Hamiltonian. This is discussed in Appendix B where we consider a simple two-level system and show the emergence of multiphoton resonances.

E. Resonances and residual electronic excited population

At resonance, the dynamics of the electronic population has a Rabi-like behavior which is completely different from the off-resonance behavior. In particular, the residual electronic population $N_{\mathbf{k},n}^{\rm res} = N_{\mathbf{k},n}(t \to \infty)$, that is the electronic population in band n at momentum $\mathbf{k}$ after the application of the pump pulse, becomes a very relevant quantity to measure and analyze. For a perfectly periodic pump pulse, that is, with infinite extension in time and no envelope, checking the l-photon resonance condition requires just the comparison of the energy gaps to $l\hbar\omega_{\rm pu}$. Instead, the presence of an envelope broadens the range of frequencies appearing in the Fourier transform of the pump pulse and hence increases the range of resonant energy gaps. To quantify this occurrence and on the basis of what reported in the previous section, we define the normalized strength of a l-photon resonance with respect to an energy gap $\varepsilon_{\rm gap}$, $w_l(\varepsilon_{\rm gap})$ as

$$w_l(\varepsilon_{\rm gap}) = e^{-\frac{\tau_{\rm pu}^2}{8\ln 2\hbar^2 l}\left(\varepsilon_{\rm gap} - l\hbar\omega_{\rm pu}\right)^2}, \quad (28)$$

where $\omega_{\rm pu}$ is the pump-pulse frequency and $\tau_{\rm pu}$ is the FWHM of its Gaussian envelope. The expression resembles the square of the amplitude of the $\varepsilon_{\rm gap}/\hbar$ component in the spectrum of the $n_{\rm ph}$th power of the pump pulse centered at $n_{\rm ph}\omega_{\rm pu}$. Then, to measure the total number of effective l-photon resonant energy gaps, W_l, it is sufficient to sum up all normalized strengths over all points $\mathbf{k}$ of the numerical momentum grid for all possible pairs of valence-conduction bands

$$W_l = \sum_{\mathbf{k},n_C,n_V} w_l\left(\varepsilon_{\mathbf{k},n_C} - \varepsilon_{\mathbf{k},n_V}\right), \quad (29)$$

where $n_C(n_V)$ runs over all conduction(valence) bands.

$N_{\mathbf{k},n_C}^{\rm res}$, the residual electronic population in one specific conduction band n_C at momentum $\mathbf{k}$, is the result of resonant processes originating in different valence bands at the same momentum $\mathbf{k}$. Each of these valence bands will contribute to $N_{\mathbf{k},n_C}^{\rm res}$ with an undetermined portion of its residual hole population $N_{\mathbf{k},n_V}^{(h)\rm res} = 1 - N_{\mathbf{k},n_V}^{\rm res}$: $\sum_{n_V} N_{\mathbf{k},n_V}^{(h)\rm res} = \sum_{n_C} N_{\mathbf{k},n_C}^{\rm res}$. Here, we suggest a procedure that allows to determine the contribution $N_{\mathbf{k},n_C,n_V}^{{\rm res}(l)}$ of the residual hole population of the valence band n_V due to a l-photon resonant process to $N_{\mathbf{k},n_C}^{\rm res}$: $N_{\mathbf{k},n_C}^{\rm res} = \sum_{l,n_V} N_{\mathbf{k},n_C,n_V}^{{\rm res}(l)}$. The rationale is to assign to each valence band n_V such a contribution, $N_{\mathbf{k},n_C,n_V}^{{\rm res}(l)}$, according to the strength of the l-photon resonant process involved, $w_l(\varepsilon_{\mathbf{k},n_C} - \varepsilon_{\mathbf{k},n_V})$, and to the actual value of $N_{\mathbf{k},n_V}^{(h)\rm res}$ with respect to those of all other

valence bands:

$$N^{\mathrm{res}(l)}_{\mathbf{k},n_C,n_V} = \frac{N^{(h)\mathrm{res}}_{\mathbf{k},n_V} w_l\left(\varepsilon_{\mathbf{k},n_C} - \varepsilon_{\mathbf{k},n_V}\right)}{\sum_{n'_V} N^{(h)\mathrm{res}}_{\mathbf{k},n'_V} \sum_{l'} w_{l'}\left(\varepsilon_{\mathbf{k},n_C} - \varepsilon_{\mathbf{k},n'_V}\right)} N^{\mathrm{res}}_{\mathbf{k},n_C}. \quad (30)$$

Given these ingredients, it is now possible to compute (i) the contribution to $N^{\mathrm{res}}_{\mathbf{k},n_C}$ coming from all l-photon resonant processes, $N^{\mathrm{res}(l)}_{\mathbf{k},n_C}$,

$$N^{\mathrm{res}(l)}_{\mathbf{k},n_C} = \sum_{n_V} N^{\mathrm{res}(l)}_{\mathbf{k},n_C,n_V}, \quad (31)$$

(ii) the contribution to $N^{\mathrm{res}}_{\mathbf{k},n_C}$ coming from each valence band n_V, $N^{\mathrm{res}}_{\mathbf{k},n_C,n_V}$,

$$N^{\mathrm{res}}_{\mathbf{k},n_C,n_V} = \sum_{l} N^{\mathrm{res}(l)}_{\mathbf{k},n_C,n_V}, \quad (32)$$

(iii) the total residual electronic population at momentum $\mathbf{k}$ coming from all l-photon resonant processes, $N^{\mathrm{res}(l)}_{\mathbf{k}}$,

$$N^{\mathrm{res}(l)}_{\mathbf{k}} = \sum_{n_V,n_C} N^{\mathrm{res}(l)}_{\mathbf{k},n_C,n_V}, \quad (33)$$

(iv) the average residual electronic population per momentum point coming from all l-photon resonant processes, $N^{\mathrm{res}(l)}$,

$$N^{\mathrm{res}(l)} = \frac{1}{M_{\mathrm{grid}}} \sum_{\mathbf{k},n_V,n_C} N^{\mathrm{res}(l)}_{\mathbf{k},n_C,n_V}, \quad (34)$$

where M_{grid} is the total number of momentum points in the numerical grid, and, finally, we can be interested in (v) the average residual excited electronic population per momentum point, N^{res}, which is actually the residual excitation population per unit cell,

$$N^{\mathrm{res}} = \frac{1}{M_{\mathrm{grid}}} \sum_{\mathbf{k},n_C} N^{\mathrm{res}}_{\mathbf{k},n_C}. \quad (35)$$

F. Generalized Houston approach

One of the model-Hamiltonian methods to simulate the behavior of pumped semiconductors is the Houston approach [27,72], which has been formulated and is generally used in first quantization and in the velocity gauge (see Appendix C). Here, we reformulate this approach in second quantization within the DPOA framework, highlighting its limitations and drawbacks.

We have seen that the Hamiltonian of a pumped quadratic lattice system has the general form $H(t) = \sum_{\mathbf{k}} H_{\mathbf{k}}(t)$ where $H_{\mathbf{k}}(t) = c^\dagger_{\mathbf{k}}(t) \odot \Xi_{\mathbf{k}}(t) \odot c_{\mathbf{k}}(t)$ and $c_{\mathbf{k}}(t_0) = (c_{\mathbf{k},1}(t_0), \ldots, c_{\mathbf{k},\nu}(t_0), \ldots)$ is the canonical operatorial basis at equilibrium in vectorial notation for an electron with momentum $\mathbf{k}$ and with ν denoting all possible degrees of freedom of the system. Let us consider the time-dependent transformation matrix $U_{\mathbf{k}}(t)$ that diagonalizes $\Xi_{\mathbf{k}}(t)$ at each instant of time, i.e., $\Xi^S_{\mathbf{k}}(t) = U^\dagger_{\mathbf{k}}(t) \odot \Xi_{\mathbf{k}}(t) \odot U_{\mathbf{k}}(t)$ has only diagonal elements that are usually called instantaneous bands. Then, we can define a new operatorial basis for the system, the Houston basis $c^S_{\mathbf{k}}(t)$, given by $c^S_{\mathbf{k}}(t) = U^\dagger_{\mathbf{k}}(t) \odot c_{\mathbf{k}}(t)$. Within the DPOA framework, we can write $c^S_{\mathbf{k}}(t) = P^S_{\mathbf{k}}(t) \odot c_{\mathbf{k}}(t_0)$ where $P^S_{\mathbf{k}}(t)$ is the Houston projection matrix that satisfies the following equation of motion:

$$i\hbar\partial_t P^S_{\mathbf{k}}(t) = \left[\Xi^S_{\mathbf{k}}(t) + \Pi_{\mathbf{k}}(t)\right] \odot P^S_{\mathbf{k}}(t), \quad (36)$$

where $\Pi_{\mathbf{k}}(t) = i\hbar\partial_t U^\dagger_{\mathbf{k}}(t) \odot U_{\mathbf{k}}(t)$. Another variant of the Houston method can be obtained, within second quantization, by the following transformation

$$P'^S_{\mathbf{k}}(t) = e^{\frac{i}{\hbar}\int_{t_0}^t dt' \Xi^S_{\mathbf{k}}(t')} \odot P^S_{\mathbf{k}}(t), \quad (37)$$

which results in the following equation of motion

$$i\hbar\partial_t P'^S_{\mathbf{k}}(t) = \Pi'_{\mathbf{k}}(t) \odot P'^S_{\mathbf{k}}(t), \quad (38)$$

where

$$\Pi'_{\mathbf{k}}(t) = e^{\frac{i}{\hbar}\int_{t_0}^t dt' \Xi^S_{\mathbf{k}}(t')} \odot \Pi_{\mathbf{k}}(t) \odot e^{-\frac{i}{\hbar}\int_{t_0}^t dt' \Xi^S_{\mathbf{k}}(t')}. \quad (39)$$

Computing $\Xi^S_{\mathbf{k}}(t)$ and $\Pi_{\mathbf{k}}(t)$, or equivalently $\Pi'_{\mathbf{k}}(t)$, is not only more time-consuming when many bands are involved as in *real* materials than just using $\Xi_{\mathbf{k}}(t)$, as in DPOA, because of the numerical diagonalizations necessary to obtain $U_{\mathbf{k}}(t)$ and $\partial_t U^\dagger_{\mathbf{k}}(t)$ at each instant of time, but it can be extremely difficult to calculate it numerically, because of the well-known difficulty of tracking the phase of eigenvectors between different instants of time in particular in the presence of instantaneous-band crossing (dynamical degeneracy) [83]. This usually leads to implementing the Houston method only for very few *effective* bands and to use *approximate* $\mathbf{k}$-independent matrix elements. Actually, DPOA can yield, if ever needed, the exact Houston-method results just computing $P^S_{\mathbf{k}}(t)$ as

$$P^S_{\mathbf{k}}(t) = U^\dagger_{\mathbf{k}}(t) \odot P_{\mathbf{k}}(t), \quad (40)$$

where $P_{\mathbf{k}}(t)$ is the usual DPOA dynamical projection matrix.

G. Inter- and intraband transitions

Within DPOA, it is straightforward to separate the effects of the so-called inter- and intraband transitions. To have only intraband transitions in the dynamics, in the basis of equilibrium bands, those indexed by n, one needs to keep only the diagonal elements of $\Xi_{\mathbf{k}}(t)$ and remove all off-diagonal ones which cause transitions among the bands:

$$i\hbar\partial_t P^{\mathrm{intra}}_{\mathbf{k},n,n'}(t) = \varepsilon^{\mathrm{intra}}_{\mathbf{k},n}(t) P^{\mathrm{intra}}_{\mathbf{k},n,n'}(t), \quad (41)$$

where $\varepsilon^{\mathrm{intra}}_{\mathbf{k},n}(t) = \Xi_{\mathbf{k},n,n}(t) = \sum_{\nu,\nu'} \Omega^\dagger_{\mathbf{k},n,\nu} \tilde{\Xi}_{\mathbf{k},\nu,\nu'}(t) \Omega_{\mathbf{k},\nu',n}$. Equation (41) has the formal solution $P^{\mathrm{intra}}_{\mathbf{k},n,n'}(t) = \delta_{n,n'} e^{-\frac{i}{\hbar}\int_{t_0}^t \varepsilon^{\mathrm{intra}}_{\mathbf{k},n}(t')dt'}$. Even though here we use the standard term *intraband transition*, one should keep in mind that performing the calculation for a specific $\mathbf{k}$ point, one does not need to take into account the equilibrium band structure or electronic distribution at any other adjacent $\mathbf{k}$ point.

However, to keep only interband transitions, it is needed to keep the off-diagonal elements of $\Xi_{\mathbf{k}}(t)$ and discard the Peierls substitution in its diagonal elements: $\varepsilon^{\mathrm{inter}}_{\mathbf{k},n}(t) = \varepsilon_{\mathbf{k},n} + e\boldsymbol{E}(t) \bullet \boldsymbol{D}_{\mathbf{k},n,n}$. Accordingly, we have

$$i\hbar\partial_t P^{\mathrm{inter}}_{\mathbf{k},n,n'}(t) = \varepsilon^{\mathrm{inter}}_{\mathbf{k},n}(t) P^{\mathrm{inter}}_{\mathbf{k},n,n'}(t) + \sum_{\bar{n}\neq n} \Xi_{\mathbf{k},n,\bar{n}}(t) P^{\mathrm{inter}}_{\mathbf{k},\bar{n},n'}(t). \quad (42)$$

Usually, the diagonal elements of the dipole matrix are negligible, $\boldsymbol{D}_{\mathbf{k},n,n} \simeq 0$, and therefore $\varepsilon^{\mathrm{inter}}_{\mathbf{k},n}(t)$ is almost equal to the equilibrium band energy $\varepsilon_{\mathbf{k},n}$.

The Houston method is often used to perform the same kind of analysis. Within the velocity gauge, to remove the intraband dynamics and define an only interband one, one sets $\mathbf{k} + \frac{e}{\hbar}\boldsymbol{A}(t) \to \mathbf{k}$ in the instantaneous eigenenergies and eigenvectors reducing them to the equilibrium ones, but one still computes the projection coefficients [see Eq. (C3)] through the full equation of motion whose interband term just comes from the differentiation of the very same Peierls-like term. This is somehow questionable and ambiguous. Moreover, defining inter- and intraband dynamics in the Houston basis is ambiguous as the instantaneous bands are superpositions of equilibrium bands and therefore any interpretation becomes very cumbersome.

H. Green's functions and TR-ARPES signal

Green's functions (GFs) are extremely important tools as they allow to compute many interesting properties of a system. The most relevant single-particle two-time electronic GFs are the retarded, G^R, and the lesser, $G^<$, GFs, defined in the vectorial notation as follows:

$$G^R_{\mathbf{k},n,n'}(t,t') = -i\theta(t-t')\langle\{c_{\mathbf{k},n}(t), c^\dagger_{\mathbf{k},n'}(t')\}\rangle, \tag{43}$$

$$G^<_{\mathbf{k},n,n'}(t,t') = i\langle c^\dagger_{\mathbf{k},n'}(t')c_{\mathbf{k},n}(t)\rangle. \tag{44}$$

Even for a quadratic Hamiltonian, the GFs cannot be computed within the SPDM approach (unless one defines a two-time SPDM [56], which is computationally very heavy), but they can be straightforwardly obtained within DPOA in terms of the dynamical projection matrices P as

$$G^R_{\mathbf{k},n,n'}(t,t') = -i\theta(t-t')\sum_m P_{\mathbf{k},n,m}(t)P^\star_{\mathbf{k},n',m}(t'), \tag{45}$$

$$G^<_{\mathbf{k},n,n'}(t,t') = i\sum_{m,m'}(\delta_{m,m'} - \rho_{\mathbf{k},m,m'}(t_0))P_{\mathbf{k},n,m}(t)P^\star_{\mathbf{k},n',m'}(t'), \tag{46}$$

where, in the band basis in which the equilibrium Hamiltonian is diagonal, $\delta_{n,n'} - \rho_{\mathbf{k},n,n'}(t_0) = \delta_{n,n'}f_+(\varepsilon_{\mathbf{k},n})$.

At equilibrium, the usual way to study the energy bands of the system, $\varepsilon_{\mathbf{k},n}$, and their corresponding occupations, is to compute the spectral functions through the imaginary components of the retarded and of the lesser GFs, respectively. However, out-of-equilibrium, the spectral functions are not necessarily nonnegative quantities [70] (see Appendix D). This occurrence invalidates their physical interpretation of availability and occupation of the corresponding energies per momentum. Nevertheless, such an information is of crucial importance to describe and understand the response of the system to external probes.

Indeed, out of equilibrium, one investigates the TR-ARPES signal [84–87], which individuates the occupation of the energy ω at momentum $\mathbf{k}$ for a probe pulse centered at time $t_{\rm pr}$. The TR-ARPES signal is proportional to

$$I^<_{\mathbf{k}}(\omega, t_{\rm pr}) = \frac{\tau_{\rm pr}}{\sqrt{8\pi\ln 2}}\int_{-\infty}^{+\infty}dt_1\int_{-\infty}^{+\infty}dt_2 S_{\rm pr}(t_1-t_{\rm pr}) S_{\rm pr}(t_2-t_{\rm pr})\mathrm{Im}[e^{i\omega(t_1-t_2)}\mathrm{Tr}[G^<_{\mathbf{k}}(t_1,t_2)]], \tag{47}$$

where $S_{\rm pr}(t-t_{\rm pr}) = \frac{2\sqrt{\ln 2}}{\sqrt{\pi}\tau_{\rm pr}}e^{-4\ln 2(t-t_{\rm pr})^2/\tau^2_{\rm pr}}$ is the probe-pulse envelope which is assumed to be Gaussian with a FWHM $\tau_{\rm pr}$. Here we assumed that the TR-ARPES matrix elements are just constant numerical factors and removed them from the expression. Moreover, we assumed that the ejected photoelectrons outside of the sample, originating from orthogonal electronic states inside of the solid, are described by orthogonal wave functions. This assumption leads to the presence of the trace (Tr) in Eq. (47). At any rate, $\mathrm{Tr}[G^<_{\mathbf{k}}(t_1,t_2)]$ is invariant with respect to the chosen basis as it is desirable. Without such assumptions, one would need to carry on a detailed modeling to get the actual matrix elements [86,87]. We have chosen the normalization factor in such a way that $I^<(\omega, t_{\rm pr})$ is normalized to the total number of particles at momentum $\mathbf{k}$,

$$\int_{-\infty}^{+\infty}d\omega I^<_{\mathbf{k}}(\omega, t_{\rm pr}) = \sum_n N_{\mathbf{k},n}. \tag{48}$$

$I^<_{\mathbf{k}}(\omega, t_{\rm pr})$ gives information about the occupied states. Instead, to identify the available states $(\omega, \mathbf{k})$, that is the bands out-of-equilibrium or TR-ARPES *bands*, we use the retarded GF in place of the lesser one and define

$$I^R_{\mathbf{k}}(\omega, t_{\rm pr}) = -\frac{\tau_{\rm pr}}{\sqrt{2\pi\ln 2}}\int_{-\infty}^{+\infty}dt_1\int_{-\infty}^{+\infty}dt_2 S_{\rm pr}(t_1-t_{\rm pr}) S_{\rm pr}(t_2-t_{\rm pr})\mathrm{Im}\big[e^{i\omega(t_1-t_2)}\mathrm{Tr}\big[G^R_{\mathbf{k}}(t_1,t_2)\big]\big]. \tag{49}$$

It is straightforward to show that, in the band basis (see Appendix E),

$$I^<_{\mathbf{k}}(\omega, t_{\rm pr}) = \sum_{n,n'}L_{\mathbf{k},n;n'}(\omega, t_{\rm pr})f_+(\varepsilon_{\mathbf{k},n'}), \tag{50}$$

$$I^R_{\mathbf{k}}(\omega, t_{\rm pr}) = \sum_{n,n'}L_{\mathbf{k},n;n'}(\omega, t_{\rm pr}), \tag{51}$$

where

$$L_{\mathbf{k},n;n'}(\omega, t_{\rm pr}) = \frac{\tau_{\rm pr}}{2\sqrt{2\pi\ln 2}}\left|\int_{-\infty}^{+\infty}dt_1 S_{\rm pr}(t_1-t_{\rm pr})e^{i\omega t_1}P_{\mathbf{k},nn'}(t_1)\right|^2, \tag{52}$$

which guarantees that the TR-ARPES signal is always nonnegative.

Equations (50) and (51) provide a generalized fluctuation-dissipation theorem for TR-ARPES signal.

III. TWO-BAND LATTICE SYSTEM: A NOTEWORTHY APPLICATION

Very recently, we have proved the capabilities of DPOA in investigating *real* materials by exploiting it to analyze the actual photoinjection mechanisms in germanium within an ultrafast (attosecond) pump-probe setup [30]. To discuss the variety of possible physical phenomena without being limited by the characteristics of a single particular *real* material, here we choose to study a toy model. This study will be a guideline for understanding the complex effects and interplays in realistic setups. We consider a cubic lattice system, of lattice constant a, with two bands corresponding to the main valence and conduction bands in a semiconductor. We consider two localized states with the onsite energies $\tilde{T}_{\mathbf{R}=\mathbf{0},1,1} = -1.65\Delta$ and $\tilde{T}_{\mathbf{R}=\mathbf{0},2,2} = 1.35\Delta$, respectively, diagonal first-neighbor hoppings $\tilde{T}_{\mathbf{R}=\boldsymbol{a},1,1} = 0.2\Delta$ and $\tilde{T}_{\mathbf{R}=\boldsymbol{a},2,2} = -0.15\Delta$, and off-diagonal first-neighbor hoppings $\tilde{T}_{\mathbf{R}=\boldsymbol{a},1,2} =$

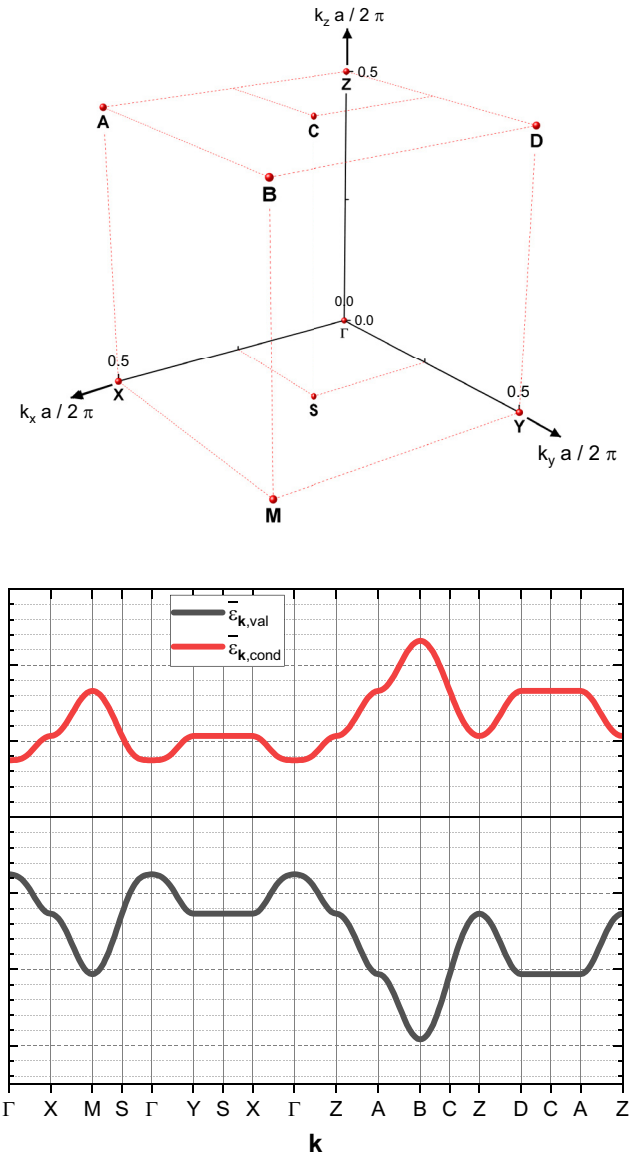

FIG. 1. (Top) High-symmetry points in the first Brillouin zone. (Bottom) Equilibrium energy bands, $\bar{\varepsilon}_{\mathbf{k},\mathrm{val}}$ and $\bar{\varepsilon}_{\mathbf{k},\mathrm{cond}}$, along the *main* path.

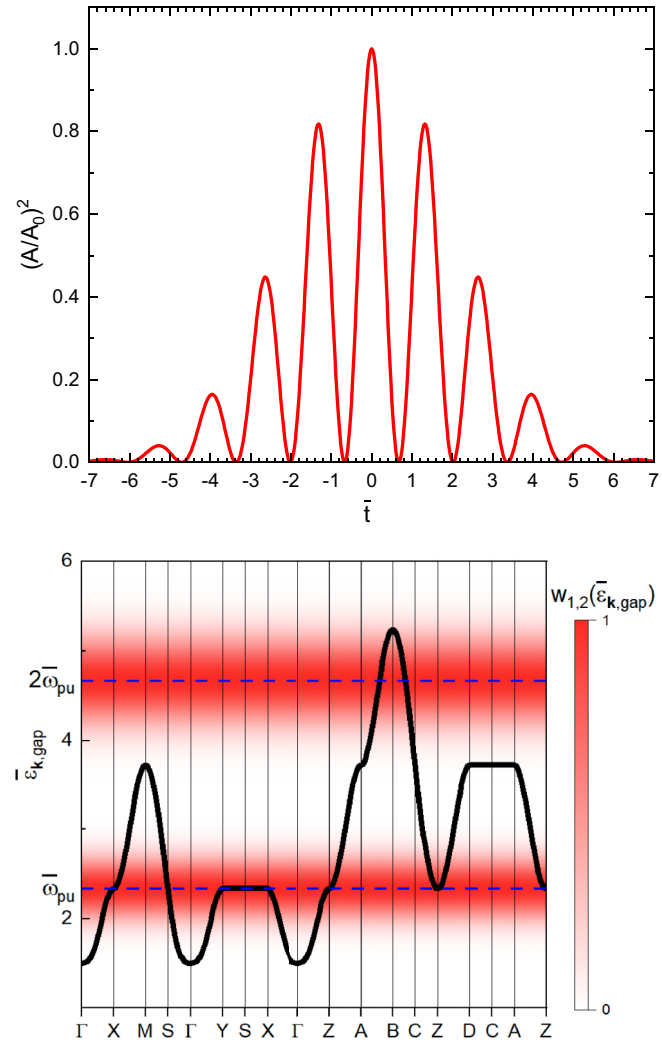

FIG. 2. (Top) The square of the pumping vector potential as a function of time. (Bottom) The energy gaps, $\bar{\varepsilon}_{\mathbf{k},\mathrm{gap}}$, along the *main* path. The colored map shows $w_{l=1,2}(\bar{\varepsilon}_{\mathbf{k},\mathrm{gap}})$ for one- and two-photon resonances.

$\tilde{T}_{\mathbf{R}=\boldsymbol{a},2,1} = -0.1\Delta$, where $\tilde{T}_{\boldsymbol{R},\nu,\nu'}$ is the hopping matrix between two sites at distance $\boldsymbol{R}$ and states ν and ν', respectively, $\boldsymbol{a} \in \{a(\pm1,0,0), a(0,\pm1,0), a(0,0,\pm1)\}$ and Δ is the unit of energy that can be adjusted to obtain the desired band gap energy at $\Gamma = (0,0,0)$. With our parameters, the band gap at Γ is 1.5Δ, so that to have a gap of 0.75 eV for instance, one should set $\Delta = 0.5$ eV. For the cases that we analyze with a finite dipole, we consider an on-site (local) and off-diagonal dipole moment: $\tilde{\mathbf{D}}_{\mathbf{R}=\mathbf{0},1,2} = \tilde{\mathbf{D}}^{*}_{\mathbf{R}=\mathbf{0},2,1} = i0.05a\hat{\mathbf{j}}$, which will lead only to a zeroth term in its *Peierls expansion*.

In Fig. 1, top panel, we show the high-symmetry points of the first Brillouin zone, while in the bottom panel we show the equilibrium energy bands, $\bar{\varepsilon}_{\mathbf{k},\mathrm{val}} = \varepsilon_{\mathbf{k},1}/\Delta$ and $\bar{\varepsilon}_{\mathbf{k},\mathrm{cond}} = \varepsilon_{\mathbf{k},2}/\Delta$, for a path which connects these high-symmetry points (the *main* path hereafter). All energies denoted with a bar on top are divided by Δ and hence dimensionless. Having Δ as the unit of energy, the unit of time is simply chosen to be $\hbar/\Delta$, which results in the dimensionless time $\bar{t} = t\Delta/\hbar$ for each time t.

We apply a pump pulse in the form $\boldsymbol{A}(\bar{t}) = A(\bar{t})\hat{\mathbf{j}}$ where $A(\bar{t})$ is a wave packet given by

$$A(\bar{t}) = \frac{2\pi\hbar}{ae}\bar{A}_0 e^{-(4\ln 2)\bar{t}^2/\bar{\tau}_{\mathrm{pu}}^2}\cos(\bar{\omega}_{\mathrm{pu}}\bar{t}), \tag{53}$$

in which the center of the pump pulse is taken as the origin of the time axis. The dimensionless frequency of the pump pulse is chosen to be $\bar{\omega}_{\mathrm{pu}} = \omega_{\mathrm{pu}}\hbar/\Delta = 2.33$ and, unless otherwise explicitly stated, the FWHM is chosen to be $\bar{\tau}_{\mathrm{pu}} = 7$ and the dimensionless pump-pulse amplitude is chosen to be $\bar{A}_0 = 0.2$.

The square of the pumping vector potential as a function of time is plotted in Fig. 2, top panel. Figure 2 bottom panel shows the energy gaps, $\bar{\varepsilon}_{\mathbf{k},\mathrm{gap}} = \bar{\varepsilon}_{\mathbf{k},\mathrm{cond}} - \bar{\varepsilon}_{\mathbf{k},\mathrm{val}}$, at the $\mathbf{k}$ points along the *main* path, while the colored map shows $w_{l=1,2}(\bar{\varepsilon}_{\mathbf{k},\mathrm{gap}})$, which indicates the strength of l-photon resonance for each energy gap.

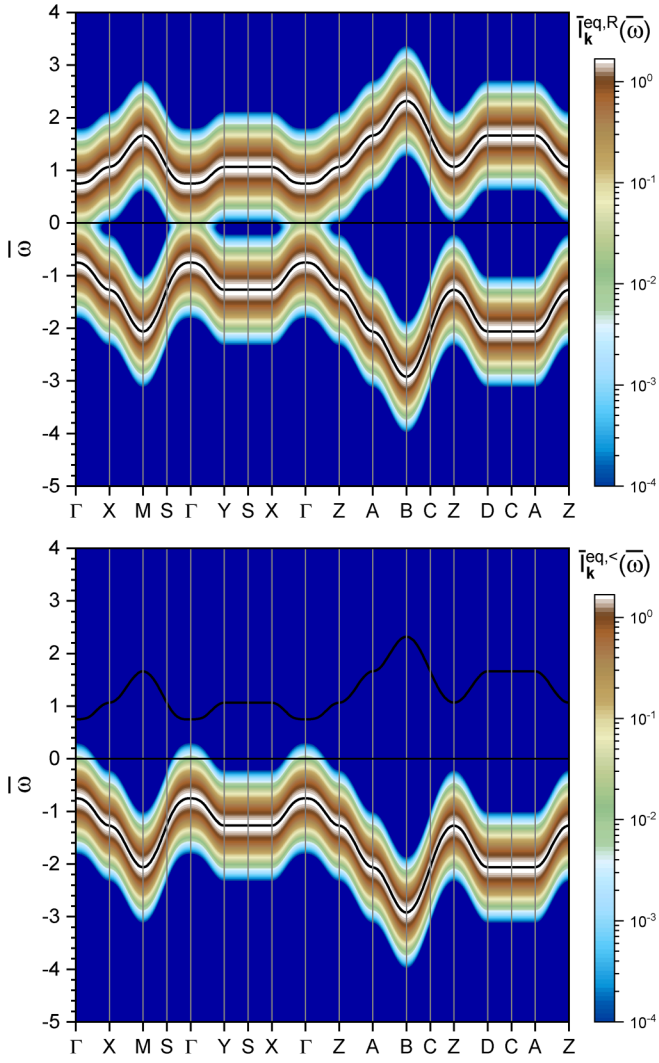

FIG. 3. TR-ARPES signals at equilibrium, (top) $\bar{I}^{eq,R}_{\mathbf{k}}(\bar{\omega})$ and (bottom) $\bar{I}^{eq,<}_{\mathbf{k}}(\bar{\omega})$. The solid black curves show the equilibrium energy bands.

For TR-ARPES signal, we apply a probe pulse with FWHM of $\bar{\tau}_{pr} = \bar{\tau}_{pu} = 7$, unless otherwise explicitly stated. We study the dimensionless signals that are obtained as $\bar{I}^{R,<}_{\mathbf{k}} = {}^{\Delta}/_{\hbar} I^{R,<}_{\mathbf{k}}$. In Fig. 3, we show $\bar{I}^{eq,R}_{\mathbf{k}}(\bar{\omega})$ and $\bar{I}^{eq,<}_{\mathbf{k}}(\bar{\omega})$ at equilibrium, that is when no pump pulse is applied to the system. The finite width of the probe pulse results in a broadening of the levels, which is intrinsic to quantum mechanics and unavoidable. Increasing the FWHM of the probe pulse, one can decrease this broadening, but we are not interested in probe pulses much wider than the pump-pulse envelope. The retarded signal, $\bar{I}^{eq,R}_{\mathbf{k}}(\bar{\omega})$, is peaked around both valence and conduction band energies and shows the spectrum of the system, while the lesser signal, $\bar{I}^{eq,<}_{\mathbf{k}}(\bar{\omega})$, shows the occupied valence-band levels only, which is the signal measured in experiments.

A. Local dipole coupling (no Peierls substitution)

As first case, we consider a Hamiltonian in which the coupling to the pumping field comes only through a local dipole moment, i.e., we neglect the Peierls substitution in the hopping term and in the dipole one [in Eq. (16) we set $\mathbf{k} + \frac{e}{\hbar}\boldsymbol{A}(t) \to \mathbf{k}$], to focus only on the effects of such a coupling on the system and analyze them in detail. This case is relevant to systems such as quantum dots and molecules, and low-dimensional systems with transverse pumps.

In Fig. 4, we show the maps of TR-ARPES signals along the *main* path. The left panel shows the retarded signal, $\bar{I}^{R}_{\mathbf{k}}(\bar{\omega}, \bar{t}_{pr} = 0)$, for the case where the center of the probe pulse coincides with the center of the pump pulse. The valence and conduction bands are more broad than at equilibrium (Fig. 3) because the electrons get excited to the conduction band and cannot be assigned to a specific band anymore, inducing a quantum-mechanical uncertainty in the energy of the bands themselves.

The photon sidebands (PSBs) emerge at energies that differ from the main-band energies of integer multiples of the (dressed) pump-pulse photon energy. Some PSBs overlap in energy with the conduction and the valence bands and, therefore, are not distinguishable in the map of the retarded signal.

On top of the maps, we reported both the equilibrium band energies (black solid curves) and the local maxima in energy of the signals at each $\mathbf{k}$ (green dots), that indicate the (out-of-equilibrium) bands of TR-ARPES. As the retarded signal shows, the equilibrium valence and conduction bands coincide with TR-ARPES ones: a local dipole, for realistic intensities, has negligible effects on the TR-ARPES bands of the system.

Since in equilibrium only the valence band is occupied, the lesser signal, $\bar{I}^{<}_{\mathbf{k}}(\bar{\omega}, \bar{t}_{pr} = 0)$, which is reported in the middle panel of Fig. 4, shows only the valence band and its corresponding PSBs. Wherever (in $\mathbf{k}$ space) we have a one-photon resonance, the related resonant one-photon PSB is definitely stronger than other PSBs as it coincides with the conduction band in this case. The two-photon PSBs are some orders of magnitude weaker than the one-photon ones and, in the scale we have chosen for the maps, it is not possible to see them.

If we probe the system after the pump pulse is turned off, i.e., by setting a large $\bar{t}_{pr} \to +\infty$, but still much shorter than the timescale of other decoherence and recombination processes like spontaneous emission or electron-phonon interaction, the spectrum of the system goes back to equilibrium, so that we have $\bar{I}^{R}_{\mathbf{k}}(\bar{\omega}, \bar{t}_{pr} \to +\infty) = \bar{I}^{R}_{\mathbf{k}}(\bar{\omega}, \bar{t}_{pr} \to -\infty)$, which is already shown in Fig. 3 and we do not repeat here.

In Fig. 4, right panel, we report $\bar{I}^{<}_{\mathbf{k}}(\bar{\omega}, \bar{t}_{pr} \to +\infty)$: contrarily to what happens for the retarded signal, the lesser signal shows residual effects at the $\mathbf{k}$ points for which the pump-pulse frequency is in one-photon resonance with the equilibrium gap energy. The multiphoton PSBs do not show any residual signal even though at $\bar{t}_{pr} = 0$ they are nonvanishing. This is because we have only a local dipole in the interaction Hamiltonian and such a term have no $\cos(l\bar{\omega}_{pu}\bar{t})$ term for $l > 1$, hence no multiphoton Rabi-like resonances. Moreover, the local dipole term we considered is completely off-diagonal, and we have no oscillating diagonal term to result in multiphoton resonances (see Appendix B). According to our experience, this can be overcome having more than two bands in the system (not shown).

In Fig. 5, top panel, we plot the residual excited electronic population in the conduction band, $N^{res}_{\mathbf{k},cond}$, for the $\mathbf{k}$ points along the *main* path as a function of the pump-pulse

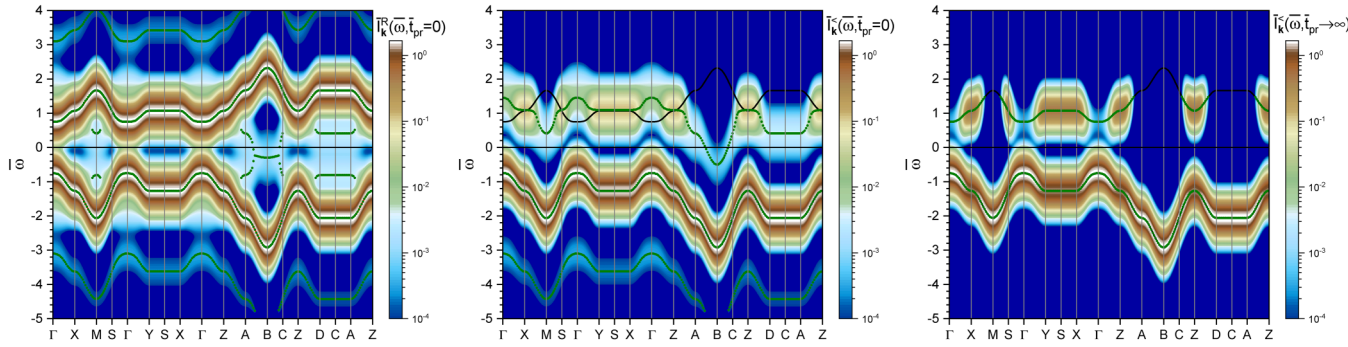

FIG. 4. TR-ARPES signals for the case of local dipole coupling. (Left) $\bar{I}^R_{\mathbf{k}}(\bar{\omega}, \bar{t}_{\rm pr} = 0)$ and (middle) $\bar{I}^<_{\mathbf{k}}(\bar{\omega}, \bar{t}_{\rm pr} = 0)$: the center of the probe pulse coincides with the center of the pump pulse. (right) $\bar{I}^<_{\mathbf{k}}(\bar{\omega}, \bar{t}_{\rm pr} \to \infty)$: after the pump pulse is turned off. The black solid curves mark the equilibrium band energies. The green dots indicate the local maxima in energy of the signals for each $\mathbf{k}$: the (out-of-equilibrium) bands of TR-ARPES.

amplitude. Rabi-like oscillations induce residual excited populations at the $\mathbf{k}$ points for which a one-photon resonance condition is realized. The finite width of the pump pulse broadens the resonant energies so that, in addition to the exact resonances, also the $\mathbf{k}$ points in the proximity of resonant ones have some residual excited population (compare with Fig. 2).

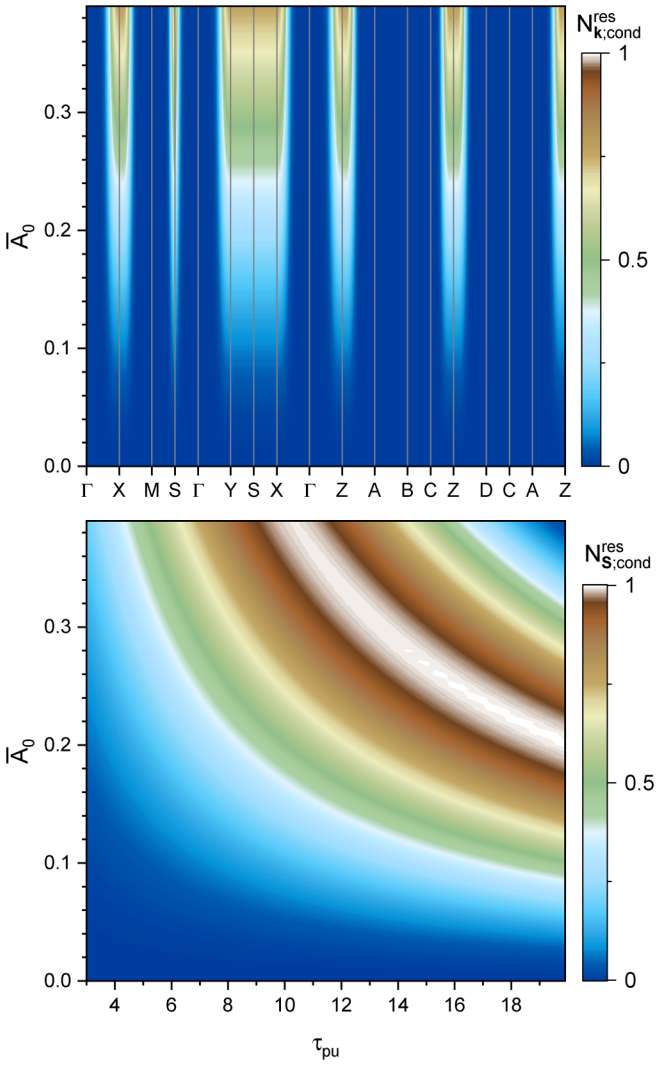

FIG. 5. Local dipole coupling case: (top) Residual excited electronic population along the *main* path as a function of the pump-pulse amplitude. (bottom) Residual excited electronic population at $\mathbf{S}$ as a function of the amplitude and of the FWHM of the pump pulse.

In Fig. 5, bottom panel, we plot the residual excited population in the conduction band at $\mathbf{S}$ as a function of the amplitude and of the FWHM of the pump pulse. Being (i) the Rabi frequency, ω_R, proportional to the pump-pulse amplitude and (ii) the overall oscillation time roughly proportional to the FWHM of the pump pulse, the residual excited population is almost constant wherever $\bar{A}_0\bar{\tau}_{\rm pu}$ is constant, that yields the hyperbolic shape of the color contours in the figure. For the very same reason, on both cuts at fixed $\bar{A}_0$ and at fixed $\bar{\tau}_{\rm pu}$, one clearly sees the *signature* of the Rabi-like oscillations. For instance, at fixed $\bar{A}_0$, that is at fixed ω_R, the end tail (in time) of the pump-pulse envelope determines the residual excited population and on changing $\bar{\tau}_{\rm pu}$ one can *scan* the Rabi-like oscillating behavior of the population [roughly $N^{\rm res}_{\mathbf{k};\rm cond} \propto \sin^2(\omega_R\tau_{\rm pu})$]. It is worth reminding that, for small $\omega_R\tau_{\rm pu}$, which is usually the more relevant case in ultrafast experiments, one can approximate $\sin(\omega_R\tau_{\rm pu}) \simeq \omega_R\tau_{\rm pu}$, which results in $N^{\rm res}_{\mathbf{k};\rm cond} \propto \bar{A}_0^2\bar{\tau}_{\rm pu}^2$.

B. Peierls substitution in hopping (no dipole)

In this case, we consider an interaction with the pump pulse via the Peierls substitution in the hopping term and set the dipole to zero. This is very relevant as the dipole term is often negligible in many realistic cases. Moreover, neglecting the dipole we can focus on the effects of band symmetries on TR-ARPES signal and electronic excitations and analyze them in detail.

In Fig. 6 top-left (top-right), we show the map of $\bar{I}^R_{\mathbf{k}}(\bar{\omega}, \bar{t}_{\rm pr} = 0)$ [$\bar{I}^<_{\mathbf{k}}(\bar{\omega}, \bar{t}_{\rm pr} = 0)$]. The higher local maxima of the TR-ARPES signal, that one can consider the main TR-ARPES bands, are slightly shifted with respect to the equilibrium valence and conduction bands and show almost no correspondence to the instantaneous eigenenergies at time zero. This is expected since TR-ARPES measures the system over a time period and not at a specific instant of time. We will shed more light on this issue later on (Fig. 14 and related discussion). For the retarded signal, which shows the full TR-ARPES spectrum of the system, we can see both valence and

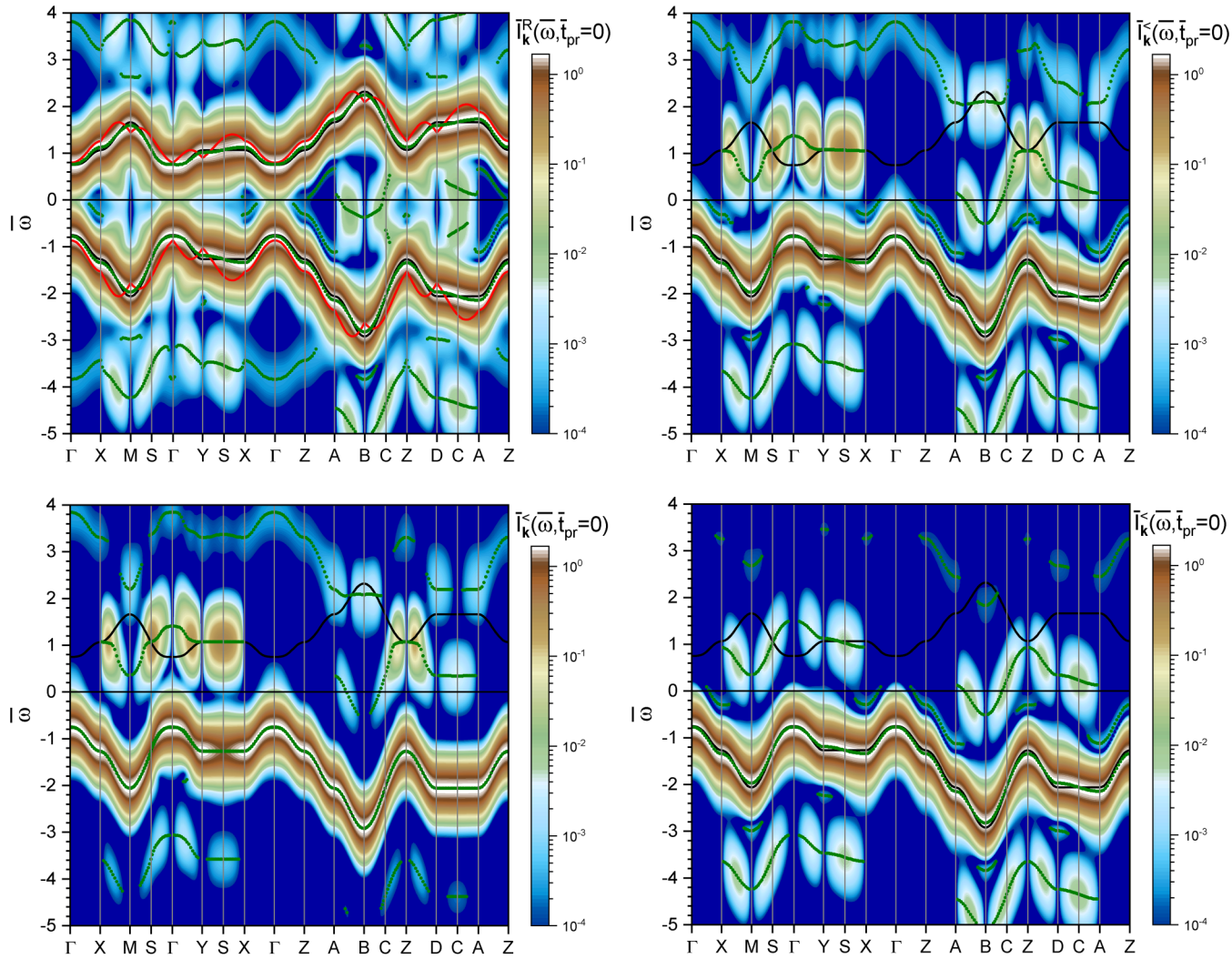

FIG. 6. TR-ARPES signals along the *main* path for Peierls substitution in the hopping term and no dipole, with the center of probe pulse coinciding with the one of pump pulse ($\bar{t}_{\rm pr} = 0$). (top-left) $\bar{I}^R_{\mathbf{k}}(\bar{\omega}, \bar{t}_{\rm pr} = 0)$ and (top-right) $\bar{I}^<_{\mathbf{k}}(\bar{\omega}, \bar{t}_{\rm pr} = 0)$ for the full dynamics, (bottom-left) $\bar{I}^<_{\mathbf{k}}(\bar{\omega}, \bar{t}_{\rm pr} = 0)$ for the dynamics with interband-only transitions, and (bottom-right) $\bar{I}^<_{\mathbf{k}}(\bar{\omega}, \bar{t}_{\rm pr} = 0)$ for the dynamics with intraband-only transitions. The black-solid curves show the equilibrium band energies while the green dots indicate the local maxima of the signals for each **k** point, which are the (out-of-equilibrium) bands of TR-ARPES. The red-solid curves show the instantaneous eigenenergies at time zero.

conduction bands and all of their sidebands. Because of the finite broadening of the bands, they overlap and distinguishing them in the case of retarded signal can be very difficult. Obviously, in the lesser signal, we see only the valence band and its sidebands.

The one-photon PSBs originate from the velocity term in the *Peierls expansion*, which is proportional to $\sin(ak_y)$ and, therefore, identically vanishes on the planes **Γ**-**X**-**A**-**Z** and **Y**-**M**-**B**-**D**, yielding no one-photon PSB there. Instead, on **S**, **C**, middle points of the lines **X**-**M**, **A**-**B**, **Z**-**D** and **Γ**-**Y**, the second order (inverse-mass) term—as well as all other even terms—of the *Peierls expansion* vanishes as it is proportional to $\cos(ak_y)$. Recall that the polarization of the pump-pulse has been chosen along the y direction.

However, even though at some of these points the two-photon PSBs are very weak, at some others (such as **S**), where we have a strong one-photon PSB, the two-photon PSB is also strong, which shows that the second order signal is assisted by multiple actions of the first order terms of the Hamiltonian (as in the case of Floquet staircase). At the **k** points where the band gap is at either one- or two-photon resonance with the pump pulse, the corresponding PSB is much stronger than non resonant ones, provided that it is not zero by symmetry.

At the **k** points where the inverse-mass vanishes, we have practically no shift of the TR-ARPES bands with respect to the equilibrium ones. The shift in the bands is mainly due to the nonoscillating components that appear in the even order terms of *Peierls expansion* [$\sum_{m=1}^{\infty} \Theta_{0,m}(t)$ in Eq. (26)], which identically vanish when the inverse-mass term vanishes by symmetry. Moreover, the higher order effects of the same term result in some weak sidebands near the main bands as it is more clear in the map of $\bar{I}^<_{\mathbf{k}}(\bar{\omega}, \bar{t}_{\rm pr} = 0)$ (top-right panel). It is worth noting that if we had an infinitely oscillating pump pulse without an envelope (that is, a pump-pulse FWHM extremely longer than the probe-pulse FWHM), there would have been no higher order effects and the nonoscillating components would have just resulted in rigid shifts of the bands. Therefore, we dub these new sidebands as envelope-Peierls

sidebands (EPSBs): they are due to both the envelope and the even terms of *Peierls expansion*. However, according to our experience, EPSBs can also result from the odd terms of the *Peierls expansion* in multiband systems.

In Fig. 6, bottom-left (bottom-right) panel, we show the map of $\bar{I}^{<}_{\mathbf{k}}(\bar{\omega}, \bar{t}_{\rm pr} = 0)$ for the dynamics with interband-only (intraband-only) transitions. Interestingly, the main TR-ARPES bands are practically on top of the equilibrium ones in the case of interband-only dynamics. However, for the case of intraband-only dynamics, we see the same shift as for the full dynamics. This is consistent with the interband transitions governing the electronic transitions between the bands and not altering the bands noticeably, while the intraband transitions change the band energies dynamically. As we already mentioned above, the shift in the main bands have the same origin as the EPSBs and since we do not have band shifts for interband-only transitions, the EPSBs disappear as well.

PSBs have different behaviors depending on being one-photon or two-photon, and in resonance or off resonance. The resonant PSBs are much stronger in the interband-only case (bottom-left panel) than in the intraband-only case (bottom-right panel), because to differentiate between in resonance and off resonance, one needs the interband transitions. On the contrary, the off-resonant one-photon PSBs are stronger in the intraband-only case than in the interband-only one, which shows that for the system parameters that we have chosen, out of resonance, the interband transitions have very negligible effects on the system, while intraband transitions obviously still induce one-photon PSBs. In fact, in the intraband-only case, our system is equivalent to a single-band (the valence band) Floquet one as the conduction band is obviously empty and not coupled to the valence band. However, in our system, in the interband-only case (bottom-left panel), two-photon off-resonance PSBs can be noticeable in comparison to the case of full dynamics (top-right panel).

The resonant one-photon (two-photon) PSBs are stronger (weaker) in the case of interband-only dynamics than in the case of the full dynamics. This can be understood by noticing that removing intraband transitions pins down the electrons at one-photon resonant **k** points and helps them to get more and more excited, while lack of the assistance provided by the intraband motions to the interband transitions, reduces the two-photon resonant PSBs. In Appendix B, it is shown that oscillating diagonal terms in a Hamiltonian, which are the origin of intraband transitions, yield another mechanism for multiphoton resonant transitions.

Another important property to be studied is the residual signal of TR-ARPES. As we already mentioned, after the action of pump pulse, the spectrum which is given by the retarded signal is exactly the one of equilibrium (Fig. 3), while the lesser signal is different. As shown in Fig. 7 top panel, where we plot $\bar{I}^{<}_{\mathbf{k}}(\bar{\omega}, \bar{t}_{\rm pr} \to \infty)$, at the one- or two-photon resonant **k** points we have the corresponding residual signals at PSBs, unless the PSB is prohibited by symmetry. For instance, this condition realizes for one-photon PSBs at **X**, **Y**, and **Z**, where we have exact one-photon resonances, and for two-photon PSBs at the middle of **A**-**B** and at **C**, where we have nonexact two-photon resonances.

Figure 7 bottom panel, shows the residual lesser signal for the dynamics given by interband-only transitions. The one-

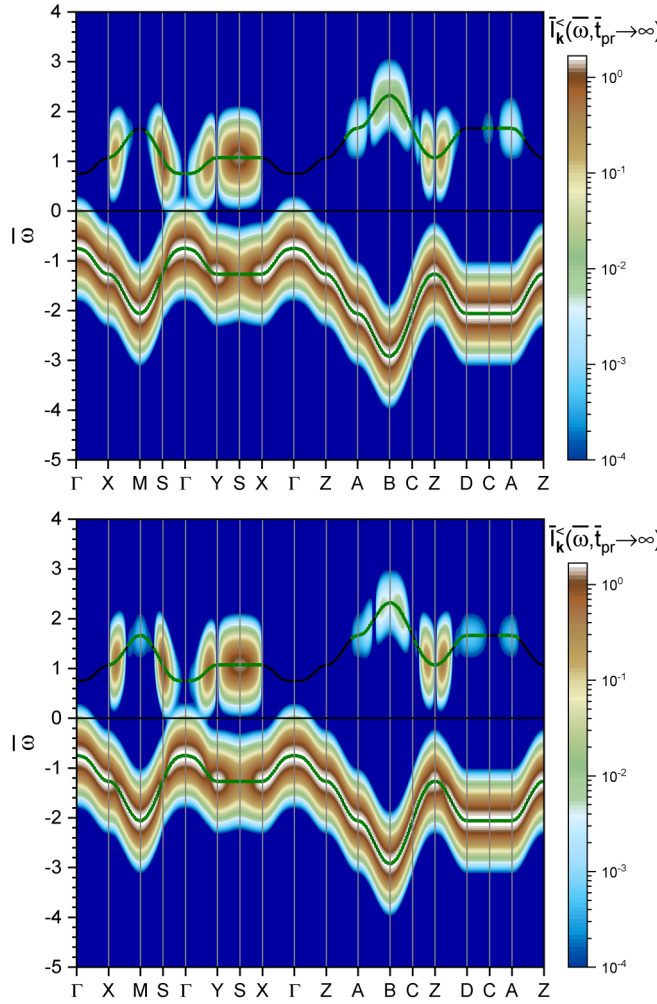

FIG. 7. Residual lesser TR-ARPES signal along the *main* path for only Peierls substitution with zero dipole, considering (top) full dynamics, and (bottom) interband-only dynamics. The black-solid curves show the equilibrium band energies while the green dots show the local maximum of the signals for a fixed **k** point.

photon (two-photon) residual PSBs are stronger (weaker) for the interband-only dynamics than for the full one according to the very same reasoning reported above. It is noteworthy that even though the intraband-only transitions induce PSBs within the pump-pulse envelope (see Fig. 6, bottom-right panel), they yield no residual in the TR-ARPES signal, which return to equilibrium after the pump pulse is turned off (Fig. 3).

In Fig. 8, top panel, we plot the residual excited populations along the *main* path as a function of the pump-pulse amplitude. One- and two-photon resonances have residual excited populations that show Rabi-like oscillations with respect to changing the pump-pulse amplitude. Moreover, unlike in the former case (only local dipole), **k** points with the same gap energies (for example those along the path **Y**-**S**-**X**) have different behaviors as their velocities and inverse-masses are different, which yields different couplings to the pumping field. In particular, at the **k** points where we have one-photon (two-photon) resonances, but the velocity (inverse mass) vanishes (see the related discussion above on the TR-ARPES

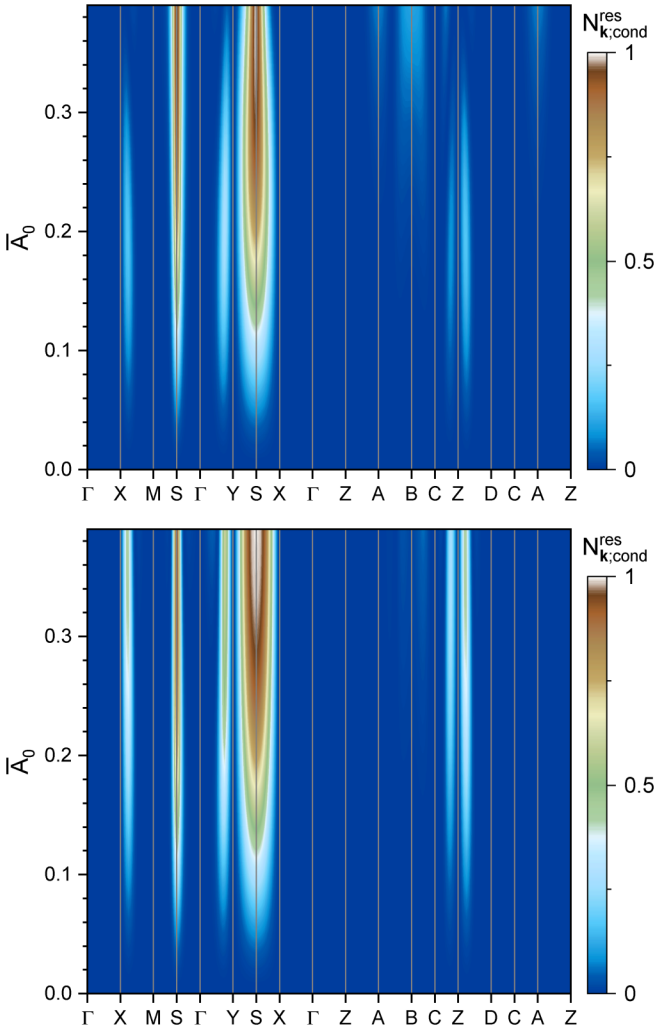

FIG. 8. Residual excitations along the *main* path as a function of the pump-pulse amplitude for the case of Peierls substitution in the hopping term and zero dipole. (Top) The full dynamics. (Bottom) The dynamics considering interband transitions only.

signal regarding the relevant regions of first Brillouin zone), there are no residual excitations. However, the points at their immediate proximities with nonexact resonant gaps, but nonzero velocities (inverse masses), host some residual excited populations.

In Fig. 8, bottom panel, we see that for the case of a dynamics with just the interband transitions, the residual excited population coming from one-photon resonances gets larger (on the contrary, if one keeps only the intraband transitions, then there would be no excitations at all). In this case, one-photon resonances get stronger because we have removed the intraband transitions that drive them transiently out of resonance and leads to a smaller residual excited population. However, there are some weak one-photon resonances that benefit from intraband transitions since they are far from the exact resonant points and by the intraband transitions they can get transiently closer to resonance. The net effect for them is to gain some residual excited population so that the related resonant region in **k**-space appears wider compared to the case of interband-only transitions. An example can be

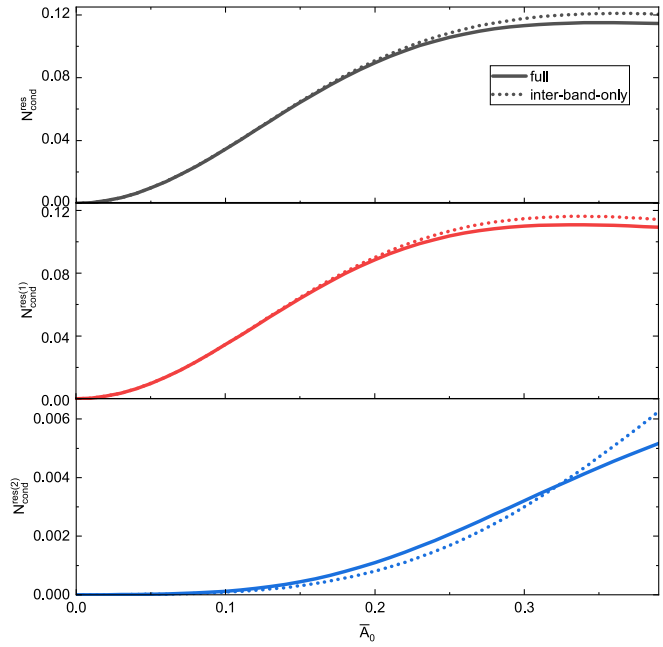

FIG. 9. Residual excited population per unit cell as a function of the pump-pulse amplitude for an $8 \times 8 \times 8$ **k** grid over the first Brillouin zone, considering Peierls substitution in the hopping term and no dipole. (top) all (any-photon) resonant contributions, (middle) only one-photon resonant contributions and (bottom) only two-photon resonant contributions. In all panels, we report the two cases of the full original Hamiltonian (solid) and interband-only Hamiltonians (dots).

the proximities of the **S** point on the path **M**-**S**-**Γ**. However, for the two-photon resonances considering only the interband transitions results in smaller residual excited populations. The two-photon resonances are assisted by the intraband transitions, similar to TR-ARPES signal (see above).

In Fig. 9, top panel, we plot the total residual excited population per unit cell, Eq. (35), as a function of the pump-pulse amplitude. We have considered an $8 \times 8 \times 8$ k-grid to sample the first Brillouin zone, even though we checked the robustness of the results with respect to the size of the grid by using also $16 \times 16 \times 16$ and $32 \times 32 \times 32$ k-grids for a larger step in the pump-pulse amplitude (not shown). We compare the two cases: the full Hamiltonian and the one with interband transitions only. For all values of the pump-pulse amplitude, the total residual excited population with only interband transitions is larger. The middle (bottom) panel of Fig. 9, shows the contribution from one-photon (two-photon) resonances, i.e., Eq. (34) with $l = 1$ ($l = 2$). In our system, the largest contribution comes from the one-photon resonances (middle panel). Computing the relative multiphoton resonance strengths [see Eq. (29)] in our grid, we find out that the relative strength of one-photon ($l = 1$) resonances is 64%, while for two-photon ($l = 2$) resonances is 36% [$W_l/(W_1 + W_2)$, see Eq. (29)]. Clearly, these numbers do not take into account the actual strength of the system-pump couplings at these resonant **k** points and that the second order transitions are generally weaker than the first order ones.

As we already explained above in detail, for the one-photon resonances (middle panel), the removal of intraband

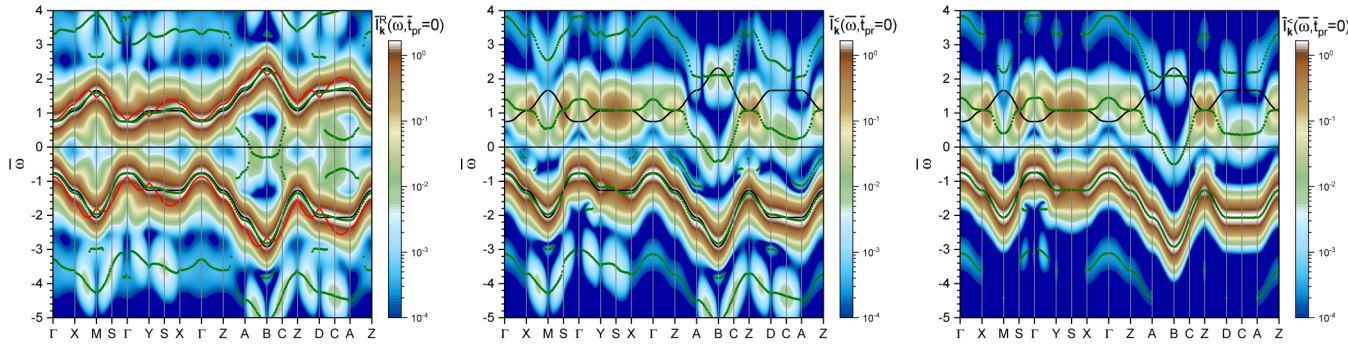

FIG. 10. The TR-ARPES signal considering both Peierls substitution and local dipole in the Hamiltonian, with the probe and pump pulses having the same center, i.e., $\bar{t}_{\rm pr} = 0$. (right) The retarded signal, (middle) the lesser signal, and (left) the lesser signal for interband-only transitions. The black-solid curves show the equilibrium band energies while the green dots show the local maxima of the signals for a fixed **k** point. The red-solid curves show the instantaneous eigenenergies at time zero.

transitions increases the residual excited populations, while for the two-photon resonances (bottom panel), the residual excited populations get reduced by removal of the intraband transitions. In the latter case, increasing the pump-pulse amplitude to high values, the behavior changes and the results of interband-only Hamiltonian overcome the full Hamiltonian ones. This can be understood by noting that, upon removing intraband transitions, the Rabi-like oscillations become in average slower over all of the two-photon resonant **k** points and of the sinlike shape we see only the monotonously increasing behavior that eventually manages to overcome the usual bending-over sinlike behavior in the case of the full Hamiltonian. This results in a higher residual excitation for very high amplitudes of the pump pulse in the case of interband-only and two-photon resonances. It is noteworthy that such very high pump-pulse intensities are not affordable in realistic setups as they would damage the sample.

C. Both Peierls substitution and local dipole

In this section, we consider both local dipole and Peierls substitution with the related Hamiltonian parameter values given in the former two cases. In this case, even though some of the effects can be explained by simply considering the mere addition of the effects yielded by the individual coupling terms, we see that the interplay between the two interaction terms is also relevant.

The retarded TR-ARPES signal along the *main* path at $\bar{t}_{\rm pr} = 0$ is shown in Fig. 10, left panel, while the lesser TR-ARPES signal is shown in the middle panel. The local dipole strengthens both one-photon and two-photon PSBs. In this case, the **k** points with zero velocity do have one-photon PSBs, because of the local dipole which does not follow the symmetry of the bands. The TR-ARPES bands are definitely closer to the equilibrium bands rather than to the instantaneous eigenenergies. The presence of both coupling terms augments the broadening of the signals as it increases the excited population overall and, in particular, at the main resonant **k** point, **S**.

Looking at the interband-only lesser TR-ARPES signal, which is shown in the right panel, we see similar behaviors to the case of zero dipole, except for one main difference: the reduction in the two-photon resonant signal is much stronger. As explained above (see also Appendix B), the intraband transition term assists the two-photon interband resonances. The addition of the local dipole term to the Peierls substitution strengthens the interband transition (stemming from off-diagonal terms in the Hamiltonian) and, in turn, makes even more effective the assistance mechanism.

It is worth noticing that we considered the local dipole to be just of interband form, therefore, the intraband-only results are exactly the same as the case of zero dipole, which were presented in Fig. 6, bottom-right panel.

In Fig. 11 top panel, we plot the residual excited population along the *main* path versus the pump-pulse amplitude. The first important change with respect to the zero dipole case is that the one-photon resonant **k** points with zero velocity (**X**, **Y**, and **Z**) do have residual excited population now: the symmetry protection is lost in the presence of the dipole term (as discussed for the TR-ARPES signal). Moreover, having both local dipole and Peierls substitution increases the Rabi frequency on the line **X**-**S**-**Y** which yields the residual excited population at **S** to have a maximum at around the pump-pulse peak amplitude of $\bar{A}_0 \simeq 0.19$, showing more clearly the Rabi-like behavior.

In Fig. 11 bottom panel, we plot the residual excited population keeping only interband transitions in the dynamics. Removing the intraband transitions, noticeably increases the residual excited population at the resonance points near **X** and **Y**, so that they can also reach the maximum of full population inversion. Moreover, for the two-photon resonant **k** points, the difference between full and interband-only dynamics is much larger than in the case of zero dipole (as discussed for TR-ARPES signal).

After investigating the residual excitation on the *main* path, we discuss the excitation per unit cell, which is obtained using an $8 \times 8 \times 8$ **k** grid to sample the first Brillouin zone and plotted in the top panel of Fig. 12. Comparison with the two former cases of considering no Peierls substitution and having zero dipole (both shown in the same panel), we see the maximum occurs at a smaller pump-pulse amplitude, as the local dipole adds up to the Peierls substitution which increases the Rabi frequencies. Another relevant feature is related to only-interband transitions in the dynamics that seem to reduce the residual excited population, which is apparently in contradiction with the result of Fig. 9. However, the behav-

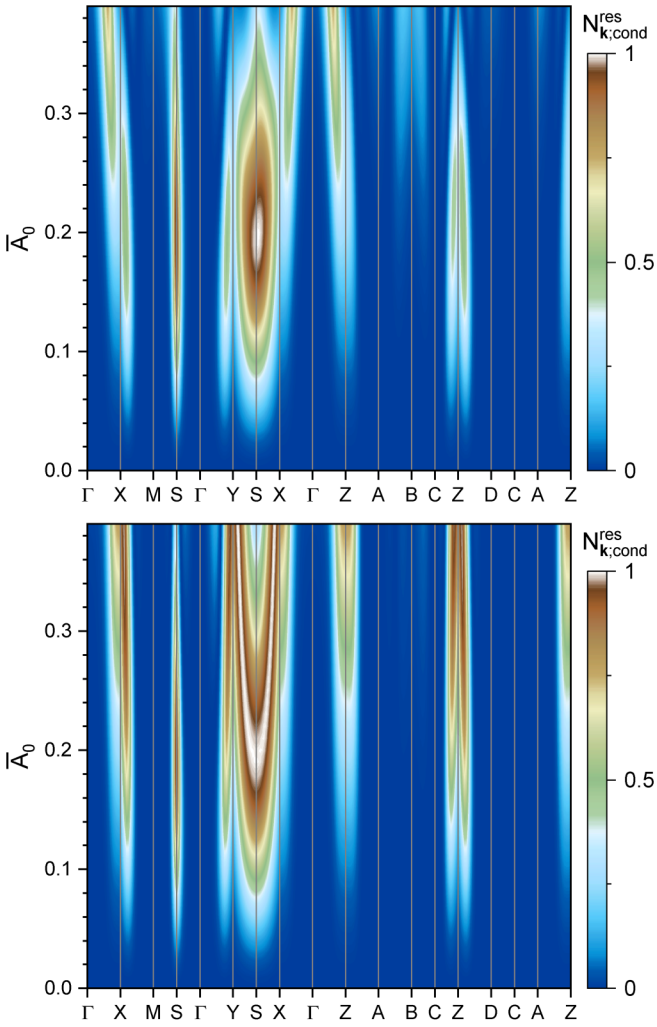

FIG. 11. Residual excitation along the *main* path as a function of the pump-pulse amplitude for the case of both Peierls substitution and local dipole. (Top) Full dynamics, (bottom) dynamics with interband transitions only.

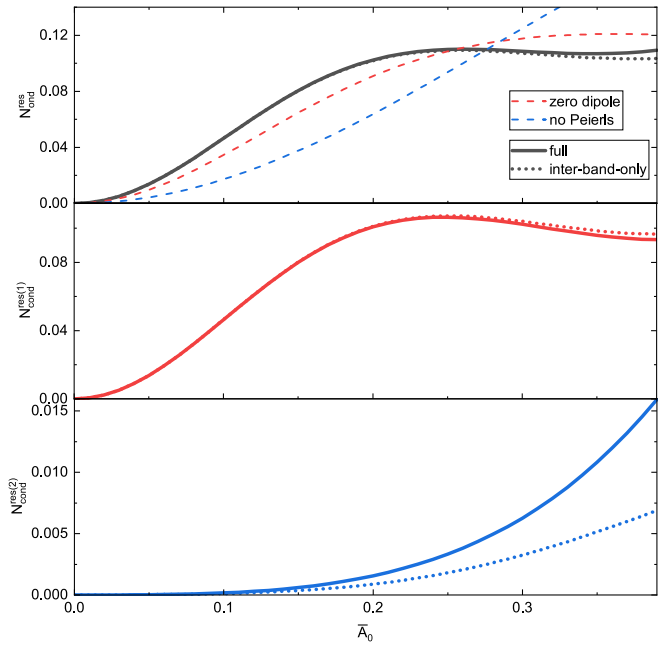

FIG. 12. Residual excitation per unit cell as a function of the pump-pulse amplitude for an $8 \times 8 \times 8$ **k** grid over the first Brillouin zone, considering both Peierls substitution and local dipole. (Top) All (any-photon) resonant contributions, (middle) one-photon, and (bottom) two-photon resonance contributions. In all panels, we report the two cases of the full original Hamiltonian (solid) and interband-only Hamiltonians (dots). In the top panel, the results of zero dipole (red dashed) and Peierls-substitution-only (blue dashed) cases are also reported.

ior of one-photon and two-photon resonance contributions, as plotted in the middle and bottom panels of Fig. 12, reveals that similar to the case of zero dipole, the interband-only dynamics gives more (less) residual excited population for the one-photon (two-photon) resonance contributions, but the difference between the interband-only and full dynamics of the two-photon resonances are much larger in this case, as we explained in the discussion of Fig. 10.

D. More on the characteristics of the TR-ARPES signal

In this section, we get more insights about the behavior of the system out of equilibrium by changing the probe-pulse parameters. For the coupling Hamiltonian, we consider both local dipole and Peierls substitution, but the general conclusions we will draw are independent of this choice.

First, we study how the TR-ARPES signal changes on varying the center of probe pulse, $\bar{t}_{pr}$, from before to after the pump-pulse envelope. The retarded and lesser TR-ARPES signals for two high-symmetry **k** points, **Γ** and **S**, are reported in Fig. 13, top panels. For both **k** points, the PSBs are detected as soon as the probe-pulse center enters the pump-pulse envelope, that is when the instantaneous eigenenergies become different from the equilibrium band energies.

At equilibrium, as expected, the lesser signal (bottom panels) shows that the electrons reside in the valence band, while they get excited into the conduction band during the pump-pulse application. At **S**, which is exactly one-photon resonant, we register an almost complete population inversion.

After the pump pulse is turned off, the residual signal at **Γ** is very weak (**Γ** is not in resonance), while at **S** we have a very strong residual signal because of the resonance condition. Having both local dipole and Peierls substitution, yields slightly more residual signal compared to the cases of removing one of the two coupling terms.

Moreover, at **S** that is a resonant point, we have the splitting of the valence band. Such a splitting is not visible at time $\bar{t}_{pr} = 0$, because the two wide split bands overlap with each other. Increasing either the local dipole or the pump-pulse amplitude one can see the splitting even at time $\bar{t}_{pr} = 0$ (not shown).

So far, the FWHM of the probe pulse was kept constant and equal to the one of the pump pulse, $\bar{\tau}_{pu} = \bar{\tau}_{pr} = 7$. Now, we study the effect of varying $\bar{\tau}_{pu}$ while keeping $\bar{t}_{pr} = 0$. In Fig. 14, the lesser signal is reported at an off-resonant **k** point $(0.375, 0.125, 0.5)$ (top panel) and at the resonant **k** point **S** (bottom panel). The former point is chosen to have an energy difference between the instantaneous eigenenergies at time

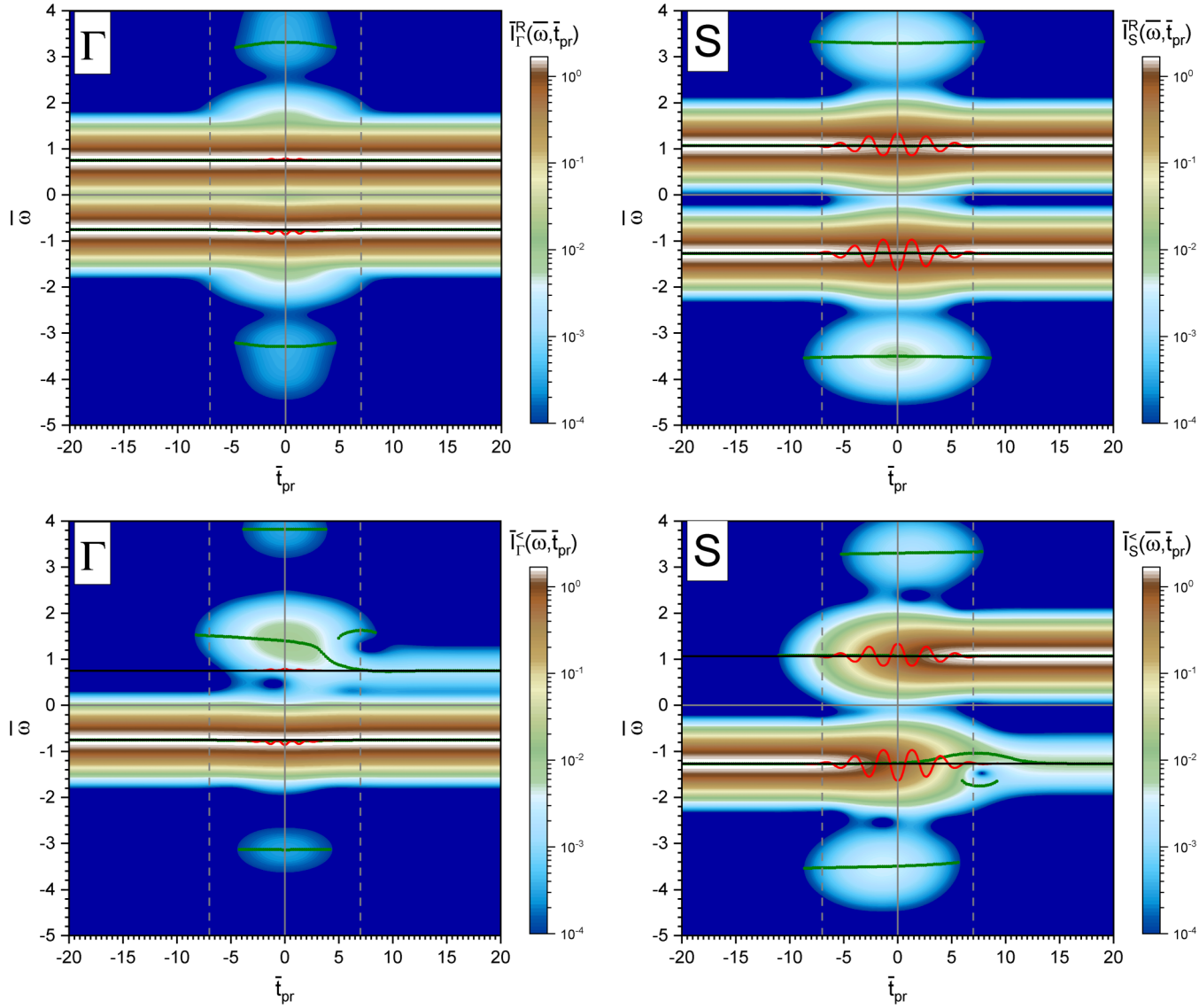

FIG. 13. (Top) The retarded and (bottom) the lesser TR-ARPES signals vs the center of probe-pulse envelope, $\bar{t}_{pr}$, for the high-symmetry points (left) **Γ** and (right) **S**. The vertical dashed gray lines determine $\pm\bar{\tau}_{pu}$. The black-solid lines show the equilibrium band energies while the green dots show the local maxima of the signals for a fixed **k** point. The red-solid curves show the instantaneous eigenenergies as functions of $\bar{t}_{pr}$.

zero and the equilibrium-band energies quite noticeable to better illustrate the phenomenology we are going to discuss.

First, we analyze the behavior at the off-resonant **k** point (top panel). For very narrow probes, that is small $\bar{\tau}_{pr}$ with respect to $\bar{\tau}_{pu}$, by decreasing $\bar{\tau}_{pr}$, the signal gets wider and its peaks tend to the instantaneous eigenenergies. This indicates that the system is practically in the lower eigenstate, which is predominantly valence-band-like as there is no excitation to the higher eigenstate. At any rate, the peaks will never exactly coincide with the instantaneous eigenenergies (even though they are very close to them) as the process is not adiabatic. We expect this also in *real* semiconductors and insulators as there the off-diagonal terms of the coupling Hamiltonian are usually much smaller than the energy gaps determined by the total Hamiltonian.

Instead, increasing the width of the probe-pulse envelope, $\bar{\tau}_{pr}$, corresponds to measuring the system over a finite time interval and, practically, to performing a time average over such an interval. This *averaging* process results in the emergence of sidebands while the main peaks tend to the equilibrium bands. The shifts of the bands are due to the high nonlinearity of the processes and to the nonzero average of the oscillating pump pulse. The PSBs remain at almost fixed energies after they emerge because they are related to the oscillating component of the pumping field, and if the probe pulse is wide enough to see the oscillations, then it does not matter how much wider it becomes. However, EPSBs change their energies by changing the width of the probe-pulse envelope, because they are driven by the nonoscillating component of the pumping field.

By increasing the width of the probe pulse to very high values, the resolution in energy increases and the peaks become

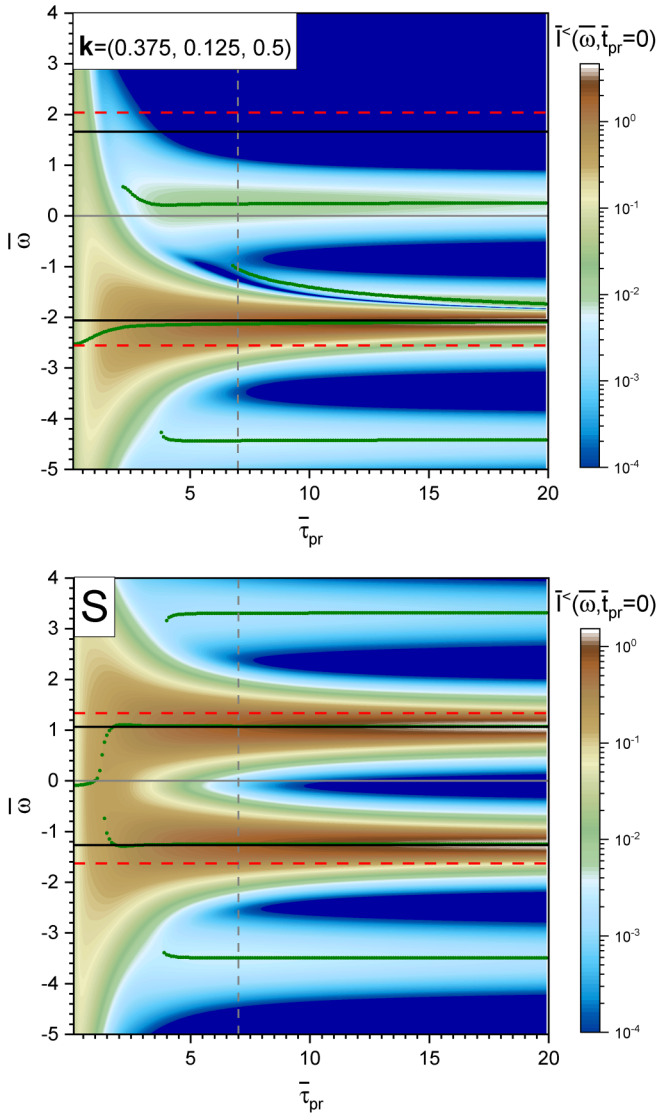

FIG. 14. The lesser TR-ARPES signals vs the FWHM of probe-pulse envelope, $\bar{\tau}_{pr}$, while the center of probe pulse is kept at $\bar{t}_{pr} = 0$, for (top) the **k** point $\mathbf{k} = (0.375, 0.125, 0.5)$ and (bottom) the high-symmetry point **S**. The vertical dashed gray lines determine $\bar{\tau}_{pu}$. The black-solid lines show the equilibrium band energies while the green dots show the local maximum of the signals for a fixed **k** point. The red-solid lines show the instantaneous eigenenergies at time zero.

very sharp. However, having such a large probe-pulse FWHM corresponds to (i) reducing more and more the time resolution of the measurement and (ii) including more and more equilibrium behavior (before pump-pulse envelope) and residual effects (after pump-pulse envelope) into the measurement. Therefore, we cannot obtain enough information about the transient out-of-equilibrium dynamics of the system. However, on decreasing the width of the probe pulse, the signals become very wide in energy. This requires more and more experimental resolution in energy to determine the position of the peaks and understand the physics. Consequently, one needs to choose some intermediate value to cope with the unavoidable intrinsic time-energy uncertainty relationship of the underlying quantum mechanical system.

The situation at resonance is quite different. As it is shown in the bottom panel of Fig. 14, even for the smallest values of $\bar{\tau}_{pu}$, the peak of lesser TR-ARPES signal does not coincide with the lower eigenenergy as the resonant dynamics forces the electrons to evolve in a superposition of valence and conduction band states. The superposition of two eigenstates results in the overlap of the TR-ARPES signals and, consequently, gives a peak somewhere in the middle of the two eigenenergies. Increasing the width of probe pulse, again the PSBs emerge and the one-photon PSB is highly populated. It is noteworthy that the inverse mass at **S** is zero and this is why we do not have any shifting of the bands and no EPSB emerges.

IV. SUMMARY AND PERSPECTIVES

In this manuscript, we have reported on a novel model-Hamiltonian approach that we have recently devised and developed to study out-of-equilibrium *real* materials [30], the dynamical projective operatorial approach (DPOA). Its internals have been illustrated in detail and the theory is extended to the calculations of TR-ARPES signal in pumped lattice systems. As a noteworthy prototypical application, a pumped two-band (valence-conduction) system, is discussed extensively. DPOA relies on many-body second-quantization formalism and composite operators to be capable of handling both weakly and strongly correlated systems. DPOA exploits the tight-binding approach and the wannierization of DFT band structures to cope with the complexity and the very many degrees of freedom of *real* materials [30]. We have devised an ad hoc *Peierls expansion* to increase the efficiency of numerical calculations. This expansion makes clear how multiphoton resonances, rigid shifts, band dressings and different types of sidebands naturally emerge and allows to understand deeply the related phenomenologies. We also reported another mechanism to explain the emergence of multiphoton resonances relaying on the intraband motion (oscillating diagonal terms in the Hamiltonian).

We have defined a protocol for evaluating the strength of single- and multiphoton resonances and for assigning the residual excited electronic population at each **k** point and band to a specific single- and multiphoton process. Comparing DPOA to the single-particle density-matrix approach and the Houston method, which we have generalized to second-quantization formalism and rephrased in the DPOA framework to compute exactly its dynamics, we have shown that DPOA goes much beyond both of them in terms of computing capabilities (multiparticle multitime correlators) and complexity handling. To study the injection processes and the out-of-equilibrium electronic dynamics, we have expressed the relevant out-of-equilibrium Green's functions and the (lesser) TR-ARPES signal within the DPOA framework. Then, defining a retarded TR-ARPES signal, which allows to analyze the behavior of the dynamical bands independently from their occupation, we have shown that it is possible to obtain an out-of-equilibrium version of the fluctuation-dissipation theorem. Another relevant aspect that we have thoroughly considered resides in the possibility to analyze intra- and interband transitions in the TR-ARPES signal and

in the residual electronic excited population by selectively inhibiting them in the model Hamiltonian.

We have studied the three most relevant cases of light-matter coupling within the dipole gauge, which has been derived in the second-quantization formalism: only a local dipole (relevant to systems such as quantum dots and molecules, and low-dimensional systems with transverse pumps), only the Peierls substitution in the hopping term (relevant to many *real* materials), and both terms at once. Within the framework of a pumped two-band lattice system, we have analyzed in detail the TR-ARPES signal and the residual electronic excited population with respect to the band energies and their symmetries as well as their dependence on the pump- and probe-pulse characteristics. We have studied: (i) how the first-order (in the pump-pulse amplitude) terms of the two types of light-matter couplings assist the higher-order ones; (ii) how their decomposition in terms of intra- and interband components can allow to understand the actual photoinjection process; (iii) how the symmetries of the system rule the actual behavior of the lesser and the retarded TR-ARPES signals as well as of the residual excited populations; (iv) how the (dynamical) bands broaden out-of-equilibrium and shift with respect to the equilibrium ones; (v) how different kinds of photon (resonant, non resonant) and envelope-Peierls sidebands emerge and vanish in relation to band symmetries and how dipole term breaks this symmetry *protection*; (vi) how residual electronic excited population accumulate in the conduction band induced by Rabi-like oscillations at the multiphoton resonant *non-symmetry-protected***k** points and the characteristics of such oscillations in terms of the pump-pulse features; (vi) how the width and the delay of the probe pulse affect the TR-ARPES signal.

Recently, we applied DPOA to unveil the different charge-injection mechanisms in ultrafast (attosecond) pumped germanium proving its efficiency and relevance to *real* experimental setups [30]. Moreover, we have obtained, within DPOA, the expressions for the time-dependent optical response (transient reflectivity and absorption) in pump-probe setups [41]. This kind of analyses is fundamental to advance the physical understanding of complex materials and the capability to eventually turn this knowledge into actual industrial and commercial applications, such as the recently proposed novel types of electronics.

ACKNOWLEDGMENTS

The authors thank C. Giannetti, M. Lucchini, S. Pittalis, and C. A. Rozzi for insightful discussions. The authors acknowledge support by Ministero dell'Istruzione, dell'Università e della Ricerca (MIUR) under Project No. PRIN 2017RKWTMY.

APPENDIX A: VELOCITY AND DIPOLE GAUGES: HAMILTONIAN, DENSITY, AND CURRENT OPERATORS

1. System

Let us start from the single-particle Hamiltonian operator in first quantization, $\hat{H}_0$, for an electron of charge $-e$ and mass m in the periodic potential $V(\mathbf{r}+\mathbf{R_i}) = V(\mathbf{r})$ generated by the Bravais lattice $\{\mathbf{R_i}\}$ of ions of a solid state system [$\mathbf{R_i} = \sum_{\lambda=1}^{3} i_\lambda \mathbf{a}_\lambda$ where $\mathbf{i} = (i_1, i_2, i_3)$, $i_\lambda \in \mathbb{Z}$ and $\mathbf{a}_\lambda$ are the lattice vectors]:

$$\hat{H}_0 = \frac{\hat{p}^2}{2m} + V(\hat{\mathbf{r}}), \tag{A1}$$

where $\hat{\mathbf{p}}$ and $\hat{\mathbf{r}}$ are the momentum and the position operators of the electron, respectively, that satisfy the canonical commutation relation $[\hat{r}_\eta, \hat{p}_{\eta'}] = i\hbar\delta_{\eta\eta'}$, where $\eta, \eta' \in \{x, y, z\}$. In this Appendix, we denote the operators in first-quantization formulation by the hat (ˆ) over-script. The Bloch theorem states that we can find a solution $|\phi_{\mathbf{k},n}\rangle = e^{i\mathbf{k}\bullet\hat{\mathbf{r}}}|u_{\mathbf{k},n}\rangle$, parametrized by the band index n and the momentum $\mathbf{k}$, of the Schrödinger equation, $\hat{H}_0|\phi_{\mathbf{k},n}\rangle = \varepsilon_{\mathbf{k},n}|\phi_{\mathbf{k},n}\rangle$, where $u_{\mathbf{k},n}(\mathbf{r}) = \langle\mathbf{r}|u_{\mathbf{k},n}\rangle$ has the periodicity of the Bravais lattice and $\varepsilon_{\mathbf{k},n}$ is the nth band-energy dispersion. We also have $\hat{H}_{0,\mathbf{k}}|u_{\mathbf{k},n}\rangle = \varepsilon_{\mathbf{k},n}|u_{\mathbf{k},n}\rangle$, where $\hat{H}_{0,\mathbf{k}} = e^{-i\mathbf{k}\bullet\hat{\mathbf{r}}}\hat{H}_0 e^{i\mathbf{k}\bullet\hat{\mathbf{r}}}$ and $\phi_{\mathbf{k},n}(\mathbf{r}) = \langle\mathbf{r}|\phi_{\mathbf{k},n}\rangle$.

2. Velocity gauge

In the dipole approximation (i.e., for wavelengths much larger than the unit cell extent in the direction of propagation), an electromagnetic wave interacting with the system (the electrons) can be described by a homogeneous vector potential $\mathbf{A}(t)$. Then, according to the minimal coupling protocol $\hat{\mathbf{p}} \to \hat{\boldsymbol{\pi}} = \hat{\mathbf{p}} + e\mathbf{A}(t)$, the Hamiltonian operator reads as

$$\hat{H} = \frac{\hat{\pi}^2}{2m} + V(\hat{\mathbf{r}}) = \hat{H}_0 + \frac{e}{m}\mathbf{A}(t)\bullet\hat{\mathbf{p}} + \frac{e^2}{2m}A^2(t), \tag{A2}$$

where $\bullet$ is the scalar product in direct space. This scenario is known as *velocity gauge* after the electron-field interaction term in the Hamiltonian: $e\mathbf{A}(\hat{\mathbf{r}}, t)\bullet\frac{\hat{\mathbf{p}}}{m}$. Let us suppose that $|\psi\rangle$ is the solution of the time-dependent Schrödinger equation, $i\hbar\frac{\partial}{\partial t}|\psi\rangle = \hat{H}|\psi\rangle$. Then, the dynamics of the charge density operator $\hat{\rho} = -e|\mathbf{r}\rangle\langle\mathbf{r}|$ and, in particular, of its average $\langle\hat{\rho}\rangle = \langle\psi|\hat{\rho}|\psi\rangle = -e|\psi(\mathbf{r}, t)|^2$ (recall that $\psi(\mathbf{r}, t) = \langle\mathbf{r}|\psi\rangle$) is given by

$$\frac{\partial}{\partial t}\langle\hat{\rho}\rangle = -\frac{i}{\hbar}\langle[\hat{\rho}, \hat{H}]\rangle = -\frac{1}{2m}\sum_{\eta=x,y,z}\nabla_\eta\langle[\hat{\rho}\hat{\pi}_\eta + \hat{\pi}_\eta\hat{\rho}]\rangle. \tag{A3}$$

Next, the continuity equation, $\frac{\partial}{\partial t}\langle\hat{\rho}\rangle + \boldsymbol{\nabla}\bullet\langle\hat{\mathbf{J}}\rangle = 0$, calls for the following definition for the current operator

$$\hat{\mathbf{J}} = \frac{1}{2m}(\hat{\rho}\hat{\boldsymbol{\pi}} + \hat{\boldsymbol{\pi}}\hat{\rho}) = \frac{1}{2m}(\hat{\rho}\hat{\mathbf{p}} + \hat{\mathbf{p}}\hat{\rho}) + \frac{e}{m}\mathbf{A}(t)\hat{\rho}, \tag{A4}$$

where we can distinguish the paramagnetic (first) and the diamagnetic (second) terms. It is worth noticing that the continuity equation can be equivalently written as follows:

$$\frac{\partial}{\partial t}\langle\hat{\rho}\rangle = \frac{i}{\hbar}\sum_{\eta=x,y,z}\langle[\hat{\pi}_\eta, \hat{J}_\eta]\rangle. \tag{A5}$$

To move to second quantization in the Bloch basis, we need

$$\begin{aligned}\mathbf{v}_{n,n'}(\mathbf{k}) &= \frac{1}{m}\langle\phi_{\mathbf{k},n}|\hat{\mathbf{p}}|\phi_{\mathbf{k},n'}\rangle \\ &= \frac{1}{\hbar}\langle u_{\mathbf{k},n}|\boldsymbol{\nabla}_\mathbf{k}\hat{H}_{0,\mathbf{k}}|u_{\mathbf{k},n'}\rangle \\ &= \delta_{nn'}\frac{1}{\hbar}\boldsymbol{\nabla}_\mathbf{k}\varepsilon_{\mathbf{k},n} - \frac{i}{\hbar}(\varepsilon_{\mathbf{k},n'} - \varepsilon_{\mathbf{k},n})\mathbf{B}_{n,n'}(\mathbf{k}),\end{aligned} \tag{A6}$$

where we have used the relation $\hat{\mathbf{p}} = -i\frac{m}{\hbar}[\hat{\mathbf{r}}, \hat{H}_0]$ and $\mathbf{B}_{n,n'}(\mathbf{k}) = \langle u_{\mathbf{k},n}|\boldsymbol{\nabla}_\mathbf{k}u_{\mathbf{k},n'}\rangle$ is the Berry connection. It is worth

noticing that the last expression requires that the Bloch basis used in the actual numerical calculations is complete. Then, we have

$$\mathcal{H} = \sum_{\mathbf{k},n,n'} \langle \phi_{\mathbf{k},n}|\hat{H}|\phi_{\mathbf{k},n'}\rangle c^\dagger_{\mathbf{k},n} c_{\mathbf{k},n'} = \sum_{\mathbf{k},n} \varepsilon_{\mathbf{k},n} c^\dagger_{\mathbf{k},n} c_{\mathbf{k},n} + \sum_{\mathbf{k},n,n'} \left(e\mathbf{A}(t) \bullet \mathbf{v}_{n,n'}(\mathbf{k}) + \delta_{nn'} \frac{e^2}{2m} A^2(t) \right) c^\dagger_{\mathbf{k},n} c_{\mathbf{k},n'}, \tag{A7}$$

where $c_{\mathbf{k},n}$ is the annihilation operator related to the single-particle state $|\phi_{\mathbf{k},n}\rangle$. We also have, in second quantization,

$$\rho(\mathbf{r}) = -e \sum_{\mathbf{k},n} |\phi_{\mathbf{k},n}(\mathbf{r})|^2 c^\dagger_{\mathbf{k},n} c_{\mathbf{k},n}, \tag{A8}$$

$$\mathbf{J}(\mathbf{r},t) = \frac{1}{2} \sum_{\mathbf{k},n,n'} |\phi_{\mathbf{k},n}(\mathbf{r})|^2 \mathbf{v}_{n,n'}(\mathbf{k}) c^\dagger_{\mathbf{k},n} c_{\mathbf{k},n'} + \frac{1}{2} \sum_{\mathbf{k},n,n'} |\phi_{\mathbf{k},n'}(\mathbf{r})|^2 \mathbf{v}_{n,n'}(\mathbf{k}) c^\dagger_{\mathbf{k},n} c_{\mathbf{k},n'} + \frac{e}{m} \mathbf{A}(t) \rho(\mathbf{r}). \tag{A9}$$

It is worth noting that, in principle, for any *real* material, $\mathbf{v}_{n,n'}(\mathbf{k})$ can be obtained through the outputs of the majority of the available DFT codes.

3. Dipole gauge

Now, we can move from computing the average of the velocity operator $\frac{1}{m}\hat{\mathbf{p}}$ and, consequently, the Berry connection, to computing the average of the operator $\hat{\mathbf{r}}$ and, therefore, the dipole operator $\hat{\mathbf{D}}$. To do that, one can apply the following unitary transformation:

$$\hat{U} = e^{-i\hat{S}}, \quad \text{where} \quad \hat{S} = -\frac{e}{\hbar} \mathbf{A}(t) \bullet \hat{\mathbf{r}}. \tag{A10}$$

Let us recall the following general relations:

$$\underline{\hat{O}} = \hat{U} \hat{O} \hat{U}^\dagger \tag{A11}$$

$$= \sum_{n=0}^{\infty} \frac{(-i)^n}{n!} [\hat{S}, [\hat{S}, \ldots, [\hat{S}, [\hat{O}]_0]_1 \ldots]_{n-1}]_n, \tag{A12}$$

$$|\underline{\psi}\rangle = \hat{U}|\psi\rangle, \quad i\hbar \frac{\partial}{\partial t} |\underline{\psi}\rangle = \overline{\hat{H}} |\underline{\psi}\rangle, \tag{A13}$$

$$\overline{\hat{H}} = \underline{\hat{H}} + \left(i\hbar \frac{\partial}{\partial t} \hat{U} \right) \hat{U}^\dagger, \tag{A14}$$

where any first-quantization operator $\hat{O}$ transformed by $\hat{U}$ is denoted by $\underline{\hat{O}}$, and $|\underline{\psi}\rangle$ is the transformation of the wave function by $\hat{U}$. The time-evolution of $|\underline{\psi}\rangle$ is given by the effective Hamiltonian $\overline{\hat{H}}$, as given in Eq. (A14), rather than $\underline{\hat{H}}$. It is straightforward to show that

$$\underline{\hat{\mathbf{r}}} = \hat{\mathbf{r}}, \tag{A15}$$

$$\underline{\hat{\mathbf{p}}} = \hat{\mathbf{p}} - e\mathbf{A}(t), \tag{A16}$$

$$\underline{\hat{\boldsymbol{\pi}}} = \hat{\boldsymbol{\pi}} - e\mathbf{A}(t) = \hat{\mathbf{p}}, \tag{A17}$$

$$\underline{\hat{H}} = \hat{H}_0, \tag{A18}$$

$$\frac{\partial}{\partial t} \hat{U} = -i \frac{e}{\hbar} (\mathbf{E}(t) \bullet \hat{\mathbf{r}}) \hat{U}, \tag{A19}$$

$$\overline{\hat{H}} = \hat{H}_0 + e\mathbf{E}(t) \bullet \hat{\mathbf{r}}, \tag{A20}$$

$$\underline{\hat{\rho}} = \hat{\rho}, \tag{A21}$$

$$\underline{\hat{\mathbf{J}}} = \hat{\mathbf{J}} - \frac{e}{m} \mathbf{A}(t) \hat{\rho} = \frac{1}{2m} (\hat{\rho}\hat{\mathbf{p}} + \hat{\mathbf{p}}\hat{\rho}), \tag{A22}$$

$$\frac{\partial}{\partial t} \langle \underline{\hat{\rho}} \rangle = -\frac{i}{\hbar} \langle [\underline{\hat{\rho}}, \overline{\hat{H}}] \rangle = -\nabla \bullet \langle \underline{\hat{\mathbf{J}}} \rangle \tag{A23}$$

$$= \frac{i}{\hbar} \sum_{\eta=x,y,z} \langle [\underline{\hat{\pi}}_\eta, \underline{\hat{J}}_\eta] \rangle, \tag{A24}$$

where $\mathbf{E}(t) = -\frac{\partial}{\partial t}\mathbf{A}(t)$ is the electric field applied to the system. It is just Eq. (A18), as sought outcome, that inspired the transformation. This scenario is known as *dipole gauge* after the electron-field interaction term in the Hamiltonian: $e\mathbf{E}(t) \bullet \hat{\mathbf{r}}$.

Moving from the Bloch states to the localized Wannier ones,

$$|\varphi_{\mathbf{i},\nu}\rangle = \frac{1}{\sqrt{N}} \sum_{\mathbf{k},n} a_{\mathbf{k},\nu,n} e^{-i\mathbf{k}\bullet\mathbf{R}_\mathbf{i}} |\phi_{\mathbf{k},n}\rangle, \tag{A25}$$

where N is generically the number of lattice sites and $a_{\mathbf{k},\nu,n}$ can be chosen to refer to a localized state (for instance, a *maximally* localized Wannier functions), $\varphi_{\mathbf{i},\nu}(\mathbf{r} - \mathbf{R}_\mathbf{i}) = \langle \mathbf{r}|\varphi_{\mathbf{i},\nu}\rangle$, around the specific Bravais lattice site $\mathbf{R}_\mathbf{i}$. Hereafter, this is the choice that has been made to properly compute the dipole term of the Hamiltonian as we will see in the following. It is easy to demonstrate that the $\hat{\mathbf{r}}$ operator has an ill-defined average on a Bravais lattice,

$$\langle \varphi_{\mathbf{i},\nu}|\hat{\mathbf{r}}|\varphi_{\mathbf{i},\nu}\rangle = \int d\mathbf{r}\mathbf{r} |\varphi_{\mathbf{i},\nu}(\mathbf{r} - \mathbf{R}_\mathbf{i})|^2 \underset{|\mathbf{R}_\mathbf{i}|\to\infty}{\to} \infty, \tag{A26}$$

implying that the Hamiltonian is also ill defined. $\langle \varphi_{\mathbf{i},\nu}|\hat{\mathbf{r}} - \hat{\mathbf{R}}|\varphi_{\mathbf{i},\nu}\rangle$ can be instead always finite if the states $|\varphi_{\mathbf{i},\nu}\rangle$ are localized enough; actually, if it is not so, then the following procedure cannot be adopted. Here, we have defined the operator $\hat{\mathbf{R}}$ as follows: $\hat{\mathbf{R}}|\varphi_{\mathbf{i},\nu}\rangle = \mathbf{R}_\mathbf{i}|\varphi_{\mathbf{i},\nu}\rangle$. Accordingly, the elements of the localized basis, $|\varphi_{\mathbf{i},\nu}\rangle$, are its eigenfunctions and the Bravais lattice sites, $\mathbf{R}_\mathbf{i}$, are the corresponding eigenvalues.

This problem calls for the application of one more unitary transformation,

$$\hat{U}' = e^{-i\hat{S}'}, \quad \text{where} \quad \hat{S}' = +\frac{e}{\hbar} \mathbf{A}(t) \bullet \hat{\mathbf{R}}. \tag{A27}$$

We can exploit the following relation to apply this transformation to the relevant operators and write them in the dipole gauge,

$$\underline{\hat{O}}_{\mathbf{i},\nu;\mathbf{j},\nu'} = \langle \varphi_{\mathbf{i},\nu}|\underline{\hat{O}}|\varphi_{\mathbf{j},\nu'}\rangle = e^{-i\frac{e}{\hbar}\mathbf{A}(t)\bullet\mathbf{R}_{\mathbf{ij}}} \underline{\hat{O}}_{\mathbf{i},\nu;\mathbf{j},\nu'}, \tag{A28}$$

and get their first-quantization form in the dipole gauge as follows:

$$\underline{\mathbf{r}}_{\mathbf{i},\nu;\mathbf{j},\nu'} = e^{-i\frac{e}{\hbar}\mathbf{A}(t)\bullet\mathbf{R}_{\mathbf{ij}}} \mathbf{r}_{\mathbf{i},\nu;\mathbf{j},\nu'}, \tag{A29}$$

$$\underline{\mathbf{p}}_{\mathbf{i},\nu;\mathbf{j},\nu'} = e^{-i\frac{e}{\hbar}\mathbf{A}(t)\bullet\mathbf{R}_{\mathbf{ij}}} [\mathbf{p}_{\mathbf{i},\nu;\mathbf{j},\nu'} - e\mathbf{A}(t)\delta_{\mathbf{i},\nu;\mathbf{j},\nu'}], \tag{A30}$$

$$\underline{\boldsymbol{\pi}}_{\mathbf{i},\nu;\mathbf{j},\nu'} = e^{-i\frac{e}{\hbar}\mathbf{A}(t)\bullet\mathbf{R}_{\mathbf{ij}}} \mathbf{p}_{\mathbf{i},\nu;\mathbf{j},\nu'}, \tag{A31}$$

$$\underline{\hat{H}}_{\mathbf{i},\nu;\mathbf{j},\nu'} = e^{-i\frac{e}{\hbar}\mathbf{A}(t)\bullet\mathbf{R}_{\mathbf{ij}}}[\hat{H}_0 + e\mathbf{E}(t)\bullet\hat{\mathbf{r}}]_{\mathbf{i},\nu;\mathbf{j},\nu'}, \tag{A32}$$

$$\frac{\partial}{\partial t}\hat{U}' = +i\frac{e}{\hbar}(\mathbf{E}(t)\bullet\hat{\mathbf{R}})\hat{U}', \tag{A33}$$

$$\overline{\overline{\hat{H}}} = \overline{\underline{\hat{H}}} + i\frac{e}{\hbar}\mathbf{E}(t)\bullet\hat{\mathbf{R}}, \tag{A34}$$

$$\overline{\overline{\hat{H}}}_{\mathbf{i},\nu;\mathbf{j},\nu'} = e^{-i\frac{e}{\hbar}\mathbf{A}(t)\bullet\mathbf{R}_{\mathbf{ij}}}[\hat{H}_0 + e\mathbf{E}(t)\bullet\hat{\mathbf{D}}]_{\mathbf{i},\nu;\mathbf{j},\nu'}, \tag{A35}$$

$$\underline{\underline{\rho}}_{\mathbf{i},\nu;\mathbf{j},\nu'} = e^{-i\frac{e}{\hbar}\mathbf{A}(t)\bullet\mathbf{R}_{\mathbf{ij}}}\rho_{\mathbf{i},\nu;\mathbf{j},\nu'}, \tag{A36}$$

$$\underline{\mathbf{J}}_{\mathbf{i},\nu;\mathbf{j},\nu'} = e^{-i\frac{e}{\hbar}\mathbf{A}(t)\bullet\mathbf{R}_{\mathbf{ij}}}\mathbf{J}_{\mathbf{i},\nu;\mathbf{j},\nu'}, \tag{A37}$$

$$\frac{\partial}{\partial t}\langle\underline{\underline{\hat{\rho}}}\rangle = -\frac{i}{\hbar}\langle[\underline{\underline{\hat{\rho}}}, \overline{\overline{\hat{H}}}]\rangle = -\nabla\bullet\langle\underline{\mathbf{J}}\rangle \tag{A38}$$

$$= \frac{i}{\hbar}\left\langle\sum_{\eta=x,y,z}[\pi_\eta, J_\eta]\right\rangle, \tag{A39}$$

where $\mathbf{R_{ij}} = \mathbf{R_i} - \mathbf{R_j}$ and $\hat{\mathbf{D}} = \hat{\mathbf{r}} - \hat{\mathbf{R}}$, and any first-quantization operator $\hat{O}$ transformed by $\hat{U}'$ is denoted by $\underline{\hat{O}}$. The transformation of the Hamiltonian $\overline{\hat{H}}$ is denoted by $\overline{\underline{\hat{H}}}$. The true effective Hamiltonian is $\overline{\overline{\hat{H}}}$, as given in Eqs. (A34) and (A35). The consecutive action of $\hat{U}$ and $\hat{U}'$ gives the operators in the dipole gauge. Moving to the second quantization, the effective Hamiltonian in the dipole gauge is written as

$$\mathcal{H} = \frac{1}{M}\sum_{\mathbf{i},\nu;\mathbf{j},\nu'}\overline{\overline{\hat{H}}}_{\mathbf{i},\nu;\mathbf{j},\nu'}\tilde{c}^\dagger_{\mathbf{i},\nu}\tilde{c}_{\mathbf{j},\nu'}. \tag{A40}$$

Substituting Eq. (A35), one obtains

$$\mathcal{H} = \frac{1}{M}\sum_{\mathbf{i},\nu;\mathbf{j},\nu'} e^{-i\frac{e}{\hbar}\mathbf{A}(t)\bullet\mathbf{R}_{\mathbf{ij}}}\tilde{T}_{\mathbf{R}_{\mathbf{ij}},\nu,\nu'}\tilde{c}^\dagger_{\mathbf{i},\nu}\tilde{c}_{\mathbf{j},\nu'} + \frac{1}{M}\sum_{\mathbf{i},\nu;\mathbf{j},\nu'} e^{-i\frac{e}{\hbar}\mathbf{A}(t)\bullet\mathbf{R}_{\mathbf{ij}}}e\mathbf{E}(t)\bullet\tilde{\mathbf{D}}_{\mathbf{R}_{\mathbf{ij}},\nu,\nu'}\tilde{c}^\dagger_{\mathbf{i},\nu}\tilde{c}_{\mathbf{j},\nu'}. \tag{A41}$$

And similarly, for the density and current operators in the dipole gauge, it is straightforward to show

$$\hat{\rho}(\mathbf{q}=\mathbf{0}) = -e\frac{1}{M}\sum_{\mathbf{i},\nu}c^\dagger_{\mathbf{i},\nu}c_{\mathbf{i},\nu} = -e\frac{N}{M}, \tag{A42}$$

$$\hat{\mathbf{J}}(\mathbf{q}=\mathbf{0},t) = i\frac{e}{\hbar}\frac{1}{M}\sum_{\mathbf{i},\nu;\mathbf{j},\nu'} e^{-i\frac{e}{\hbar}\mathbf{A}(t)\bullet\mathbf{R}_{\mathbf{ij}}}\mathbf{R}_{\mathbf{ij}}\tilde{T}_{\mathbf{R}_{\mathbf{ij}},\nu,\nu'}\tilde{c}^\dagger_{\mathbf{i},\nu}\tilde{c}_{\mathbf{j},\nu'} + i\frac{e}{\hbar}\frac{1}{M}\sum_{\mathbf{i},\nu;\mathbf{j},\nu'} e^{-i\frac{e}{\hbar}\mathbf{A}(t)\bullet\mathbf{R}_{\mathbf{ij}}}[\hat{\mathbf{D}}, \hat{H}_0]_{\mathbf{i},\nu;\mathbf{j},\nu'}\tilde{c}^\dagger_{\mathbf{i},\nu}\tilde{c}_{\mathbf{j},\nu'}, \tag{A43}$$

where

$$[\hat{\mathbf{D}}, \hat{H}_0]_{\mathbf{i},\nu;\mathbf{j},\nu'} = \sum_{\mathbf{i}',\nu''}\tilde{\mathbf{D}}_{\mathbf{R}_{\mathbf{ii}'},\nu,\nu''}\tilde{T}_{\mathbf{R}_{\mathbf{i}'\mathbf{j}},\nu'',\nu'} - \sum_{\mathbf{i}',\nu''}\tilde{T}_{\mathbf{R}_{\mathbf{ii}'},\nu,\nu''}\tilde{\mathbf{D}}_{\mathbf{R}_{\mathbf{i}'\mathbf{j}},\nu'',\nu'}, \tag{A44}$$

$\tilde{T}_{\mathbf{R}_{\mathbf{ij}},\nu,\nu'} = (\hat{H}_0)_{\mathbf{i},\nu;\mathbf{j},\nu'}$ is known as the hopping matrix, and $\tilde{\mathbf{D}}_{\mathbf{R}_{\mathbf{ij}},\nu,\nu'} = (\hat{\mathbf{D}})_{\mathbf{i},\nu;\mathbf{j},\nu'}$ is the dipole matrix. We have considered a homogeneous lattice so that both the hoping and the dipole matrices depend on the difference $\mathbf{R_{ij}}$. $\tilde{c}_{\mathbf{i},\nu}$ is the annihilation operator related to the single-particle state $|\varphi_{\mathbf{i},\nu}\rangle$, M is the number of lattice sites, N is the total number of electrons in the system, and we have used the relations $\hat{\mathbf{p}} = -i\frac{m}{\hbar}[\hat{\mathbf{r}}, \hat{H}_0]$ and $\langle\varphi_{\mathbf{i},\nu}|[\hat{\mathbf{R}}, \hat{O}]|\varphi_{\mathbf{j},\nu'}\rangle = \mathbf{R_{ij}}\hat{O}_{\mathbf{i},\nu;\mathbf{j},\nu'}$.

Then, we move to the momentum space using Fourier transformation,

$$\tilde{c}_{\mathbf{k},\nu} = \frac{1}{\sqrt{M}}\sum_{\mathbf{i}} e^{i\mathbf{k}\bullet\mathbf{R}_{\mathbf{i}}}\tilde{c}_{\mathbf{i},\nu}, \tag{A45}$$

and we obtain

$$\mathcal{H} = \sum_{\mathbf{k},\nu,\nu'}\tilde{T}_{\mathbf{k}+\frac{e}{\hbar}\mathbf{A}(t),\nu,\nu'}\tilde{c}^\dagger_{\mathbf{k},\nu}\tilde{c}_{\mathbf{k},\nu'} + e\mathbf{E}(t)\bullet\sum_{\mathbf{k},\nu,\nu'}\tilde{\mathbf{D}}_{\mathbf{k}+\frac{e}{\hbar}\mathbf{A}(t),\nu,\nu'}\tilde{c}^\dagger_{\mathbf{k},\nu}\tilde{c}_{\mathbf{k},\nu'}, \tag{A46}$$

$$\rho(\mathbf{q}=\mathbf{0}) = -e\frac{1}{M}\sum_{\mathbf{k},\nu}\tilde{c}^\dagger_{\mathbf{k},\nu}\tilde{c}_{\mathbf{k},\nu'} = -e\frac{N}{M}, \tag{A47}$$

$$\begin{aligned}\mathbf{J}(\mathbf{q}=\mathbf{0},t) &= -\frac{e}{\hbar}\sum_{\mathbf{k},\nu',\nu}\left[\nabla_{\mathbf{k}}\tilde{T}_{\mathbf{k}+\frac{e}{\hbar}\mathbf{A}(t),\nu,\nu'}\right]\tilde{c}^\dagger_{\mathbf{k},\nu}\tilde{c}_{\mathbf{k},\nu'} \\ &+ i\frac{e}{\hbar}\sum_{\mathbf{k},\nu,\nu',\nu''}\left[\tilde{\mathbf{D}}_{\mathbf{k}+\frac{e}{\hbar}\mathbf{A}(t),\nu,\nu''}\tilde{T}_{\mathbf{k}+\frac{e}{\hbar}\mathbf{A}(t),\nu'',\nu'}\right]\tilde{c}^\dagger_{\mathbf{k},\nu}\tilde{c}_{\mathbf{k},\nu'} \\ &- i\frac{e}{\hbar}\sum_{\mathbf{k},\nu,\nu',\nu''}\left[\tilde{T}_{\mathbf{k}+\frac{e}{\hbar}\mathbf{A}(t),\nu,\nu''}\tilde{\mathbf{D}}_{\mathbf{k}+\frac{e}{\hbar}\mathbf{A}(t),\nu'',\nu'}\right]\tilde{c}^\dagger_{\mathbf{k},\nu}\tilde{c}_{\mathbf{k},\nu'},\end{aligned} \tag{A48}$$

where

$$\tilde{T}_{\mathbf{k},\nu,\nu'} = \frac{1}{M}\sum_{\mathbf{i},\mathbf{j}} e^{-i\mathbf{k}\bullet\mathbf{R}_{\mathbf{ij}}}\tilde{T}_{\mathbf{R}_{\mathbf{ij}},\nu,\nu'}, \tag{A49}$$

$$\tilde{\mathbf{D}}_{\mathbf{k},\nu,\nu'} = \frac{1}{M}\sum_{\mathbf{i},\mathbf{j}} e^{-i\mathbf{k}\bullet\mathbf{R}_{\mathbf{ij}}}\tilde{\mathbf{D}}_{\mathbf{R}_{\mathbf{ij}},\nu,\nu'}, \tag{A50}$$

or equivalently

$$\tilde{T}_{\mathbf{k},\nu,\nu'} = \sum_{\mathbf{i}} e^{-i\mathbf{k}\bullet\mathbf{R}_{\mathbf{i}}}\tilde{T}_{\mathbf{R}_{\mathbf{i}},\nu,\nu'}, \tag{A51}$$

$$\tilde{\mathbf{D}}_{\mathbf{k},\nu,\nu'} = \sum_{\mathbf{i}} e^{-i\mathbf{k}\bullet\mathbf{R}_{\mathbf{i}}}\tilde{\mathbf{D}}_{\mathbf{R}_{\mathbf{i}},\nu,\nu'}. \tag{A52}$$

Again, it is worth noting that, in principle, for any *real* material, $\tilde{T}_{\mathbf{R}_{\mathbf{ij}},\nu,\nu'}$ and $\tilde{\mathbf{D}}_{\mathbf{R}_{\mathbf{ij}},\nu,\nu'}$ can be obtained as standard outputs of *Wannier90* code [80], given its interfaces to a certain number of available DFT codes.

APPENDIX B: OSCILLATIONS OF THE DIAGONAL ELEMENTS AND MULTIPHOTON RESONANCES

Let us study a simple two-level system with the equilibrium eigenstates $|1\rangle$, $|2\rangle$ and eigenenergies ε_1, ε_2, respectively. The gap frequency is $\omega_g = (\varepsilon_2 - \varepsilon_1)/\hbar > 0$. The Hamiltonian of such a system under the application of a pump pulse, has the following generic form:

$$\mathcal{H}(t) = \begin{pmatrix}\varepsilon_1(t) & \lambda_{12}(t)\\ \lambda_{21}(t) & \varepsilon_2(t)\end{pmatrix}. \tag{B1}$$

The time-dependent state of the system, $|\psi(t)\rangle$, can be spanned in the basis of equilibrium eigenstates:

$$|\psi(t)\rangle = a_1(t)|1\rangle + a_2(t)|2\rangle, \tag{B2}$$

and it is straightforward to show that

$$i\hbar\dot{a}_\alpha(t) = \varepsilon_\alpha(t)a_\alpha(t) + \lambda_{\alpha\bar{\alpha}}(t)a_{\bar{\alpha}}(t), \tag{B3}$$

where $\alpha, \bar{\alpha} \in \{1, 2\}$ and $\bar{\alpha} = (\alpha \mod 2) + 1$.

In this Appendix, we consider a perfectly periodic pump, and for simplicity, real off-diagonal terms, hence, $\lambda_{\alpha\bar{\alpha}}(t) = \lambda_0 \sin(\omega t)$.

1. Standard Rabi oscillation

For the case of standard Rabi oscillations, one considers constant diagonal terms in time, i.e., $\varepsilon_\alpha(t) = \varepsilon_\alpha$. As it is quite well known, one can obtain the dynamics by simply defining $a_\alpha(t) = a_{0,\alpha}(t)e^{-i\varepsilon_\alpha t/\hbar}$. Considering the one photon resonant condition, $\omega = \omega_g$, and the rotating wave approximation (RWA), one obtains the following EOM for $a_{0,\alpha}(t)$:

$$\ddot{a}_{0,\alpha}(t) \approx -\left(\frac{\lambda_0}{2\hbar}\right)^2 a_{0,\alpha}(t), \tag{B4}$$

which results in a Rabi oscillation with the Rabi frequency $\omega_R = \frac{\lambda_0}{\hbar}$. It is worth noticing that in this case, there is no way of getting a multiphoton resonance.

2. Oscillations of the diagonal elements

In a more general case, which is very common in realistic setups (e.g., in lattice systems), the diagonal terms of the out-of-equilibrium Hamiltonian also oscillate. One can write

$$\varepsilon_\alpha(t) = \varepsilon_\alpha + \delta_\alpha \sin(\omega t + \phi_\alpha), \tag{B5}$$

where δ_α is the amplitude of the diagonal oscillation and ϕ_α is its phase. Let us define

$$a_{0,\alpha}(t) = a_\alpha(t)e^{\frac{i}{\hbar}\left(\varepsilon_\alpha t - \frac{\delta_\alpha}{\omega}\cos(\omega t+\phi_\alpha)\right)}. \tag{B6}$$

One can straightforwardly show that

$$\begin{aligned} i\hbar\dot{a}_{0,\alpha}(t) = \lambda_0 \sin(\omega t)e^{i(\varepsilon_\alpha-\varepsilon_{\bar{\alpha}})t/\hbar} \\ e^{\frac{i}{\hbar\omega}(\delta_{\bar{\alpha}}\cos(\omega t+\phi_{\bar{\alpha}})-\delta_\alpha\cos(\omega t+\phi_\alpha))}a_{0,\bar{\alpha}}(t). \end{aligned} \tag{B7}$$

Given that our aim is to understand the general effect of the oscillating diagonal terms, we consider $\delta_1 = \delta_2 = \delta$, $\phi_1 = \pi$ and $\phi_2 = 0$, so that $\varepsilon_{1/2}(t) = \varepsilon_{1/2} \mp \delta\sin(\omega t)$. The EOM reduces to

$$i\hbar\dot{a}_{0,1/2}(t) = \lambda_0 \sin(\omega t)e^{\mp i\omega_g t}e^{\pm 2i\frac{\delta}{\hbar\omega}\cos(\omega t)}a_{0,2/1}(t). \tag{B8}$$

Expanding the term $e^{\pm 2i\frac{\delta}{\hbar\omega}\cos(\omega t)}$ and performing some algebra, one can show that

$$i\hbar\dot{a}_{0,1/2}(t) = a_{0,2/1}(t)\frac{\lambda_0}{2i}e^{\mp i\omega_g t}\sum_{n=-\infty}^{\infty}(b_{n-1,\pm\delta} - b_{n+1,\pm\delta})e^{in\omega t},$$

where

$$b_{n,\delta} = \sum_{r=0}^{\infty}\frac{1}{(2r+|n|)!}\left(i\frac{\delta}{\hbar\omega}\right)^{2r+|n|}\binom{2r+|n|}{r}. \tag{B9}$$

In this case, one can verify the emergence of Rabi-like oscillations also at multiphoton resonances. Consider a n-photon resonance condition: $\omega_g = n\omega$, and apply RWA to remove all of the fast oscillating terms. We remind the reader that here we do not want to give an analytical solution to the EOM, but our goal is to investigate the resonance conditions and the situations in which Rabi-like oscillations emerge. The EOM reduces to

$$i\hbar\dot{a}_{0,1/2}(t) \approx \frac{\lambda_0}{2i}(b_{\pm n-1,\pm\delta} - b_{\pm n+1,\pm\delta})a_{0,2/1}(t). \tag{B10}$$

Differentiating Eq. (B10) with respect to time, we get

$$\ddot{a}_{0,\alpha}(t) \approx -\left(\frac{\lambda_0}{2\hbar}\right)^2|b_{n-1,\delta} - b_{n+1,\delta}|^2 a_{0,\alpha}(t), \tag{B11}$$

which has the same form of Eq. (B4). This shows the emergence of a Rabi-like oscillatory behavior for a multiphoton resonant case, with the Rabi frequency of $\omega_R^{(n)} = \frac{\lambda_0}{\hbar}|b_{n-1,\delta} - b_{n+1,\delta}|$ where $n \geqslant 1$. As a conclusion, oscillating diagonal terms in the Hamiltonian are a possible source of multiphoton resonances.

APPENDIX C: THE HOUSTON APPROACH

One of the methods used to simulate the behavior of pumped semiconductors is the Houston approach [27,72]. Such an approach is usually formulated in the velocity gauge and first quantization, just for the reason that will become clear in the following. Let us start from the time-independent single-particle Hamiltonian of the Bloch system under analysis,

$$\hat{H}_0 = \frac{\hat{p}^2}{2m} + V(\hat{\mathbf{r}}), \tag{C1}$$

where $\hat{\mathbf{p}}$ and $\hat{\mathbf{r}}$ are the momentum and position operators, respectively, m is the electron mass, and $V(\hat{\mathbf{r}})$ is the periodic potential of the system under analysis. The related time-independent Schrödinger equation $\hat{H}_0|\psi_{\boldsymbol{k},n}\rangle = \varepsilon_{\boldsymbol{k},n}|\psi_{\boldsymbol{k},n}\rangle$ is solved in terms of the Bloch bands $\varepsilon_{\boldsymbol{k},n}$ and of the Bloch functions $|\psi_{\boldsymbol{k},n}\rangle = e^{-i\boldsymbol{k}\bullet\hat{\mathbf{r}}}|u_{\boldsymbol{k},n}\rangle$ where $|u_{\boldsymbol{k},n}\rangle$ displays the same periodicity of the potential. Accordingly, we have the following reduced equation $\hat{H}_{0,\boldsymbol{k}}|u_{\boldsymbol{k},n}\rangle = \varepsilon_{\boldsymbol{k},n}|u_{\boldsymbol{k},n}\rangle$ where $\hat{H}_{0,\boldsymbol{k}} = e^{i\boldsymbol{k}\bullet\hat{\mathbf{r}}}\hat{H}_0e^{-i\boldsymbol{k}\bullet\hat{\mathbf{r}}} = \frac{(\hat{\mathbf{p}}-\hbar\boldsymbol{k})^2}{2m} + V(\hat{\mathbf{r}})$. Now, if we have a pump pulse described by the vector potential $\mathbf{A}(t)$ impinging on the system, then the related time-dependent minimal-coupling Hamiltonian in the velocity gauge reads as

$$\hat{H}(t) = \frac{(\hat{\mathbf{p}} + e\mathbf{A}(t))^2}{2m} + V(\hat{\mathbf{r}}), \tag{C2}$$

where $e > 0$ is the electronic charge. It is straightforward to demonstrate that the eigenfunctions and the eigenvalues of this Hamiltonian are simply $|\varphi_{\boldsymbol{k},n}(t)\rangle = e^{-i\boldsymbol{k}\bullet\hat{\mathbf{r}}}|u_{\boldsymbol{k}+\frac{e}{\hbar}\mathbf{A}(t),n}\rangle$ and $\varepsilon_{\boldsymbol{k}+\frac{e}{\hbar}\mathbf{A}(t),n}$, respectively. The set of such eigenfunctions is usually named the instantaneous or the adiabatic basis because these states would exactly describe the behavior of the system only if the pump pulse would be so slowly varying on the characteristic timescales (energies) of the system to allow it to adjust to the pump pulse at each instant of time (i.e., adiabatically). Accordingly, they do not solve the general time-dependent Schrödinger equation $\hat{H}(t)|\phi_{\boldsymbol{k}}(t)\rangle =$

$i\hbar\frac{\partial}{\partial t}|\phi_{\boldsymbol{k}}(t)\rangle$, but they can be used as a basis for expanding $|\phi_{\boldsymbol{k}}(t)\rangle = \sum_n \lambda_{\boldsymbol{k},n}(t)|\varphi_{\boldsymbol{k},n}(t)\rangle$. The projection coefficients $\lambda_{\boldsymbol{k},n}(t)$ are determined via the following equation of motion:

$$i\hbar\frac{\partial}{\partial t}\lambda_{\boldsymbol{k},n}(t) = (\varepsilon_{\boldsymbol{k}+\frac{e}{\hbar}\mathbf{A}(t),n} - \theta_{\boldsymbol{k},n}(t))\lambda_{\boldsymbol{k},n}(t) + i\hbar\frac{e}{m}\sum_{n'(\neq n)}\frac{\mathbf{E}(t)\bullet\mathbf{p}_{\boldsymbol{k},n,n'}(t)}{\Delta\varepsilon_{\boldsymbol{k},n,n'}(t)}\lambda_{\boldsymbol{k},n'}(t), \quad \text{(C3)}$$

where $\theta_{\boldsymbol{k},n}(t) = \langle\varphi_{\boldsymbol{k},n}(t)|i\hbar\frac{\partial}{\partial t}|\varphi_{\boldsymbol{k},n}(t)\rangle$ is connected to the Berry phase of the system and can be neglected if there is no degeneracy, $\mathbf{p}_{\boldsymbol{k},n,n'}(t) = \langle\varphi_{\boldsymbol{k},n}(t)|\hat{\mathbf{p}}|\varphi_{\boldsymbol{k},n'}(t)\rangle$ is the matrix element of the momentum in the instantaneous basis, $\Delta\varepsilon_{\boldsymbol{k},n,n'}(t) = \varepsilon_{\boldsymbol{k}+\frac{e}{\hbar}\mathbf{A}(t),n} - \varepsilon_{\boldsymbol{k}+\frac{e}{\hbar}\mathbf{A}(t),n'}$ and $\mathbf{E}(t) = -\frac{\partial}{\partial t}\mathbf{A}(t)$ is the applied electric field. Defining new coefficients $\beta_{\boldsymbol{k},n}(t)$ such that $\lambda_{\boldsymbol{k},n}(t) = \beta_{\boldsymbol{k},n}(t)e^{-\frac{i}{\hbar}\int_{-\infty}^{t}\varepsilon_{\boldsymbol{k}+\frac{e}{\hbar}\mathbf{A}(t'),n}dt'}$, the projection-coefficient equation further simplifies to

$$i\hbar\frac{\partial}{\partial t}\beta_{\boldsymbol{k},n}(t) = -\theta_{\boldsymbol{k},n}(t)\beta_{\boldsymbol{k},n}(t) + i\hbar\frac{e}{m}\sum_{n'(\neq n)}\frac{\mathbf{E}(t)\bullet\mathbf{p}_{\boldsymbol{k},n,n'}(t)}{\Delta\varepsilon_{\boldsymbol{k},n,n'}(t)} \times e^{\frac{i}{\hbar}\int_{-\infty}^{t}\Delta\varepsilon_{\boldsymbol{k},n,n'}(t')dt'}\beta_{\boldsymbol{k},n'}(t), \quad \text{(C4)}$$

and the corresponding basis $\{e^{-\frac{i}{\hbar}\int_{-\infty}^{t}\varepsilon_{\boldsymbol{k}+\frac{e}{\hbar}\mathbf{A}(t'),n}dt'}|\varphi_{\boldsymbol{k},n}(t)\rangle\}$ is the Houston basis, which differs just by a time-dependent phase factor from the instantaneous basis (actually, both basis are often dubbed in the literature as Houston basis).

The main appeal of such a procedure resides in the possibility of obtaining sensible results even if one: (i) focuses only on few bands (e.g., one valence, one conduction and, if needed, one core band), (ii) supposes that $\mathbf{p}_{\boldsymbol{k},n,n'}(t)$ is approximately $\boldsymbol{k}$-independent so that $\mathbf{p}_{\boldsymbol{k},n,n'}(t) \approx \mathbf{p}_{n,n'}$ (the time dependence gets canceled as well), and (iii) uses the parabolic approximation $\varepsilon_{\boldsymbol{k},n} \approx \varepsilon_n + \frac{\hbar^2k^2}{2m_n}$, that is, retains only relevant gaps $|\varepsilon_n - \varepsilon_{n'}|$ and effective masses m_n in the proximity of few selected $\boldsymbol{k}$ points.

APPENDIX D: OUT-OF-EQUILIBRIUM SPECTRAL FUNCTIONS

To obtain the spectral functions, we need the Fourier transformation of the GFs with respect to time, which we perform as follows:

$$G^{R,<}_{\mathbf{k}}(\omega,t) = \int_{-\infty}^{+\infty} d\tau e^{i\omega\tau - 0^+|\tau|}G^{R,<}_{\mathbf{k}}\left(t+\frac{\tau}{2}, t-\frac{\tau}{2}\right), \quad \text{(D1)}$$

where 0^+ is an infinitesimal convergence factor. Then, the (retarded) spectral function is given by

$$A^R_{\mathbf{k}}(\omega,t) = -\frac{1}{\pi}\mathrm{Im}\left[\mathrm{Tr}G^R_{\mathbf{k}}(\omega,t)\right], \quad \text{(D2)}$$

while the lesser spectral function is defined as

$$A^<_{\mathbf{k}}(\omega,t) = \frac{1}{2\pi}\mathrm{Im}\left[\mathrm{Tr}G^<_{\mathbf{k}}(\omega,t)\right]. \quad \text{(D3)}$$

In Fig. 15, top and bottom panels, we report the dimensionless retarded and lesser functions, $\bar{A}^{R,<}_{\mathbf{k}}(\bar{\omega},t) = A^{R,<}_{\mathbf{k}}(\bar{\omega},t)\Delta/\hbar$, respectively, as function of $\bar{\omega}$ along the *main* path, for the same pump-pulse and system parameters as the ones of Fig. 6. In the left, middle, and right panels, the time t is chosen to be well before the application of the pump pulse, in the center of the pump pulse ($t = 0$), and well after the application of pump pulse, respectively. Clearly, during the application of the pump pulse, the spectral functions, $\bar{A}^{R,<}_{\mathbf{k}}(\bar{\omega},t)$, become negative and lose their original physical interpretations.

Obviously, in the absence of the pump pulse (both before and after its application), the spectral function gives correct information about the energy bands of the system. The left panel of Fig. 15 can be directly compared to Fig. 3 and the only difference to be acknowledged is that, in the former, the band broadening originates from the finite numerical value of 0^+, while, in the latter, it originates from the finite FWHM of the probe pulse. After the application of the pump pulse, the bands recover their equilibrium shape as it can be seen by comparing the top-right panel of Fig. 15 to its top-left panel. However, the lesser spectral function (see bottom-right panel of Fig. 15) shows that at some $\mathbf{k}$ points we have residual excitations similarly to what is reported in the top panel of Fig. 7.

APPENDIX E: TR-ARPES SIGNAL IN THE BAND BASIS

In this Appendix, we derive Eqs. (50) and (51) in the equilibrium band basis. Substituting Eq. (46) into Eq. (47) and using $\mathrm{Im}[z] = \frac{1}{2i}(z - z^\star)$, the lesser signal can be written as

$$I^<_{\mathbf{k}}(\omega,t_{\mathrm{pr}}) = \frac{\tau_{\mathrm{pr}}}{4\sqrt{2\pi\ln 2}}\int_{-\infty}^{+\infty}dt_1\int_{-\infty}^{+\infty}dt_2 \, S_{\mathrm{pr}}(t_1-t_{\mathrm{pr}})S_{\mathrm{pr}}(t_2-t_{\mathrm{pr}}) \times\Bigg[e^{i\omega(t_1-t_2)}\sum_{n,n'}f_+(\varepsilon_{\mathbf{k},n'})P_{\mathbf{k},n,n'}(t_1)P^\star_{\mathbf{k},n,n'}(t_2) + e^{-i\omega(t_1-t_2)}\sum_{n,n'}f_+(\varepsilon_{\mathbf{k},n'})P^\star_{\mathbf{k},n,n'}(t_1)P_{\mathbf{k},n,n'}(t_2)\Bigg]. \quad \text{(E1)}$$

Changing the dummy variable $t_1 \longleftrightarrow t_2$, one can verify that the fourth and third lines of Eq. (E1) are equal to each other. Rearranging the terms, one can simply show that

$$I^<_{\mathbf{k}}(\omega,t_{\mathrm{pr}}) = \frac{\tau_{\mathrm{pr}}}{2\sqrt{2\pi\ln 2}}\sum_{n,n'}f_+(\varepsilon_{\mathbf{k},n'})|Q_{\mathbf{k},n,n'}(\omega,t_{\mathrm{pr}})|^2, \quad \text{(E2)}$$

where

$$Q_{\mathbf{k},n,n'}(\omega,t_{\mathrm{pr}}) = \int_{-\infty}^{+\infty}dt e^{i\omega t}S_{\mathrm{pr}}(t-t_{\mathrm{pr}})P_{\mathbf{k},n,n'}(t). \quad \text{(E3)}$$

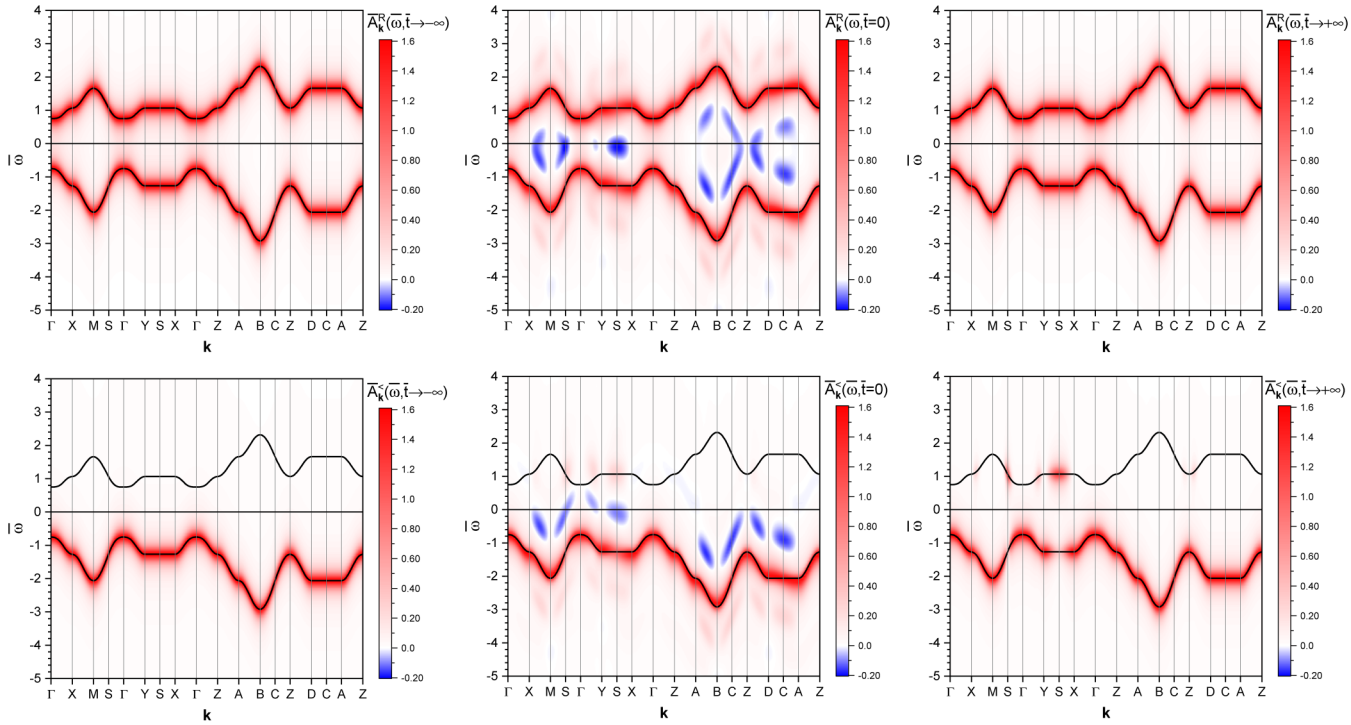

FIG. 15. Top and bottom panels: the dimensionless spectral function, $\bar{A}^R_{\mathbf{k}}(\bar{\omega}, t)$, and lesser spectral function, $\bar{A}^<_{\mathbf{k}}(\bar{\omega}, t)$, respectively, as function of ω along the *main* path, for the same pump-pulse and system parameters as the one of Fig. 6. In the left, middle, and right panels, the time t is chosen to be well before the application of pump pulse, in the center of the pump pulse ($t = 0$), and well after the application of pump pulse, respectively. The black solid curves show the equilibrium bands. The numerical value of 0^+ has been chosen to be $0.2\Delta/\hbar$.

Defining $L_{\mathbf{k},n;n'}(\omega, t_{\rm pr}) = \frac{\tau_{\rm pr}}{2\sqrt{2\pi \ln 2}} |Q_{\mathbf{k},n,n'}(\omega, t_{\rm pr})|^2$ one obtains Eq. (50).

For the retarded signal, substituting Eq. (45) into Eq. (49) and using $\mathrm{Im}[z] = \frac{1}{2i}(z - z^\star)$, we have

$$
\begin{aligned}
&I^R_{\mathbf{k}}(\omega, t_{\rm pr}) \\
&\quad = \frac{\tau_{\rm pr}}{2\sqrt{2\pi \ln 2}} \int_{-\infty}^{+\infty} dt_1 \int_{-\infty}^{+\infty} dt_2 S_{\rm pr}(t_1 - t_{\rm pr}) S(t_2 - t_{\rm pr}) \\
&\quad \times \Bigg[\theta(t_1 - t_2) e^{i\omega(t_1 - t_2)} \sum_{n,n'} P_{\mathbf{k},n,n'}(t_1) P^\star_{\mathbf{k},n,n'}(t_2) \\
&\quad + \theta(t_1 - t_2) e^{-i\omega(t_1 - t_2)} \sum_{n,n'} P^\star_{\mathbf{k},n,n'}(t_1) P_{\mathbf{k},n,n'}(t_2) \Bigg]. \qquad \text{(E4)}
\end{aligned}
$$

Changing the dummy variable $t_1 \leftrightarrow t_2$ in the last line of this align and using $\theta(t_1 - t_2) + \theta(t_2 - t_1) = 1$, we get

$$
\begin{aligned}
I^R_{\mathbf{k}}(\omega, t_{\rm pr}) = \frac{\tau_{\rm pr}}{2\sqrt{2\pi \ln 2}} &\int_{-\infty}^{+\infty} dt_1 \int_{-\infty}^{+\infty} dt_2 \\
&S_{\rm pr}(t_1 - t_{\rm pr}) S(t_2 - t_{\rm pr}) \\
&\times e^{i\omega(t_1 - t_2)} \sum_{n,n'} P_{\mathbf{k},n,n'}(t_1) P^\star_{\mathbf{k},n,n'}(t_2), \qquad \text{(E5)}
\end{aligned}
$$

which simply results in

$$
I^R_{\mathbf{k}}(\omega, t_{\rm pr}) = \frac{\tau_{\rm pr}}{2\sqrt{2\pi \ln 2}} \sum_{n,n'} |Q_{\mathbf{k},n,n'}(\omega, t_{\rm pr})|^2 \qquad \text{(E6)}
$$

and proves Eq. (51).

[1] T. Brabec and F. Krausz, Rev. Mod. Phys. **72**, 545 (2000).

[2] F. Krausz and M. Ivanov, Rev. Mod. Phys. **81**, 163 (2009).

[3] F. Krausz and M. I. Stockman, Nat. Photon. **8**, 205 (2014).

[4] F. Calegari, G. Sansone, S. Stagira, C. Vozzi, and M. Nisoli, J. Phys. B: At., Mol. Opt. Phys. **49**, 062001 (2016).

[5] R. Borrego-Varillas, M. Lucchini, and M. Nisoli, Rep. Prog. Phys. **85**, 066401 (2022).

[6] H. Aoki, N. Tsuji, M. Eckstein, M. Kollar, T. Oka, and P. Werner, Rev. Mod. Phys. **86**, 779 (2014).

[7] M. Zürch, H.-T. Chang, L. J. Borja, P. M. Kraus, S. K. Cushing, A. Gandman, C. J. Kaplan, M. H. Oh, J. S. Prell, D. Prendergast, C. D. Pemmaraju, D. M. Neumark, and S. R. Leone, Nat. Commun. **8**, 15734 (2017).

[8] M. Zürch, H.-T. Chang, P. M. Kraus, S. K. Cushing, L. J. Borja, A. Gandman, C. J. Kaplan, M. H. Oh, J. S. Prell, D. Prendergast, C. D. Pemmaraju, D. M. Neumark, and S. R. Leone, Struct. Dyn. **4**, 044029 (2017).

[9] C. J. Kaplan, P. M. Kraus, A. D. Ross, M. Zürch, S. K. Cushing, M. F. Jager, H.-T. Chang, E. M. Gullikson, D. M. Neumark, and S. R. Leone, Phys. Rev. B **97**, 205202 (2018).

[10] L. Perfetti, P. A. Loukakos, M. Lisowski, U. Bovensiepen, M. Wolf, H. Berger, S. Biermann, and A. Georges, New J. Phys. **10**, 053019 (2008).

[11] F. Schmitt, P. S. Kirchmann, U. Bovensiepen, R. G. Moore, L. Rettig, M. Krenz, J.-H. Chu, N. Ru, L. Perfetti, D. Lu *et al.*, Science **321**, 1649 (2008).

[12] D. von der Linde, T. Engers, G. Jenke, P. Agostini, G. Grillon, E. Nibbering, A. Mysyrowicz, and A. Antonetti, Phys. Rev. A **52**, R25 (1995).

[13] P. A. Norreys, M. Zepf, S. Moustaizis, A. P. Fews, J. Zhang, P. Lee, M. Bakarezos, C. N. Danson, A. Dyson, P. Gibbon, P. Loukakos, D. Neely, F. N. Walsh, J. S. Wark, and A. E. Dangor, Phys. Rev. Lett. **76**, 1832 (1996).

[14] A. H. Chin, O. G. Calderón, and J. Kono, Phys. Rev. Lett. **86**, 3292 (2001).

[15] S. Ghimire, A. D. DiChiara, E. Sistrunk, P. Agostini, L. F. DiMauro, and D. A. Reis, Nat. Phys. **7**, 138 (2011).

[16] T. T. Luu, M. Garg, S. Y. Kruchinin, A. Moulet, M. T. Hassan, and E. Goulielmakis, Nature (London) **521**, 498 (2015).

[17] S. Han, H. Kim, Y. W. Kim, Y.-J. Kim, S. Kim, I.-Y. Park, and S.-W. Kim, Nat. Commun. **7**, 13105 (2016).

[18] L. J. Borja, M. Zürch, C. D. Pemmaraju, M. Schultze, K. Ramasesha, A. Gandman, J. S. Prell, D. Prendergast, D. M. Neumark, and S. R. Leone, J. Opt. Soc. Am. B **33**, C57 (2016).

[19] Y. S. You, D. A. Reis, and S. Ghimire, Nat. Phys. **13**, 345 (2017).

[20] H. Liu, Y. Li, Y. S. You, S. Ghimire, T. F. Heinz, and D. A. Reis, Nat. Phys. **13**, 262 (2017).

[21] S. Jiang, S. Gholam-Mirzaei, E. Crites, J. E. Beetar, M. Singh, R. Lu, M. Chini, and C. Lin, J. Phys. B: At., Mol. Opt. Phys. **52**, 225601 (2019).

[22] M. Schultze, E. M. Bothschafter, A. Sommer, S. Holzner, W. Schweinberger, M. Fiess, M. Hofstetter, R. Kienberger, V. Apalkov, V. S. Yakovlev *et al.*, Nature (London) **493**, 75 (2013).

[23] L. Stojchevska, I. Vaskivskyi, T. Mertelj, P. Kusar, D. Svetin, S. Brazovskii, and D. Mihailovic, Science **344**, 177 (2014).

[24] M. Schultze, K. Ramasesha, C. Pemmaraju, S. Sato, D. Whitmore, A. Gandman, J. S. Prell, L. Borja, D. Prendergast, K. Yabana *et al.*, Science **346**, 1348 (2014).

[25] M. Lucchini, S. A. Sato, A. Ludwig, J. Herrmann, M. Volkov, L. Kasmi, Y. Shinohara, K. Yabana, L. Gallmann, and U. Keller, Science **353**, 916 (2016).

[26] H. Mashiko, K. Oguri, T. Yamaguchi, A. Suda, and H. Gotoh, Nat. Phys. **12**, 741 (2016).

[27] F. Schlaepfer, M. Lucchini, S. A. Sato, M. Volkov, L. Kasmi, N. Hartmann, A. Rubio, L. Gallmann, and U. Keller, Nat. Phys. **14**, 560 (2018).

[28] C. J. Kaplan, P. M. Kraus, E. M. Gullikson, L. J. Borja, S. K. Cushing, M. Zürch, H.-T. Chang, D. M. Neumark, and S. R. Leone, J. Opt. Soc. Am. B **36**, 1716 (2019).

[29] R. Geneaux, H. J. Marroux, A. Guggenmos, D. M. Neumark, and S. R. Leone, Phil. Trans. R. Soc. A. **377**, 20170463 (2019).

[30] G. Inzani, L. Adamska, A. Eskandari-asl, N. D. Palo, G. L. Dolso, B. Moio, L. J. D'Onofrio, A. Lamperti, A. Molle, R. Borrego-Varillas, M. Nisoli, S. Pittalis, C. A. Rozzi, A. Avella, and M. Lucchini, Nat. Photon. **17**, 1059 (2023).

[31] G. Inzani, A. Eskandari-asl, L. Adamska, B. Moio, G. L. Dolso, N. D. Palo, L. J. D'Onofrio, A. Lamperti, A. Molle, C. A. Rozzi, R. Borrego-Varillas, M. Nisoli, S. Pittalis, A. Avella, and M. Lucchini, Il Nuovo Cimento C **46**, 110 (2023).

[32] O. Neufeld, N. Tancogne-Dejean, U. De Giovannini, H. Hübener, and A. Rubio, npj Comput. Mater. **9**, 39 (2023).

[33] T. Rohwer, S. Hellmann, M. Wiesenmayer, C. Sohrt, A. Stange, B. Slomski, A. Carr, Y. Liu, L. M. Avila, M. Kalläne *et al.*, Nature (London) **471**, 490 (2011).

[34] C. L. Smallwood, J. P. Hinton, C. Jozwiak, W. Zhang, J. D. Koralek, H. Eisaki, D.-H. Lee, J. Orenstein, and A. Lanzara, Science **336**, 1137 (2012).

[35] S. Hellmann, T. Rohwer, M. Kalläne, K. Hanff, C. Sohrt, A. Stange, A. Carr, M. Murnane, H. Kapteyn, L. Kipp *et al.*, Nat. Commun. **3**, 1069 (2012).

[36] E. Papalazarou, J. Faure, J. Mauchain, M. Marsi, A. Taleb-Ibrahimi, I. Reshetnyak, A. van Roekeghem, I. Timrov, N. Vast, B. Arnaud, and L. Perfetti, Phys. Rev. Lett. **108**, 256808 (2012).

[37] Y. Wang, H. Steinberg, P. Jarillo-Herrero, and N. Gedik, Science **342**, 453 (2013).

[38] J. C. Johannsen, S. Ulstrup, F. Cilento, A. Crepaldi, M. Zacchigna, C. Cacho, I. C. Edmond Turcu, E. Springate, F. Fromm, C. Raidel, T. Seyller, F. Parmigiani, M. Grioni, and P. Hofmann, Phys. Rev. Lett. **111**, 027403 (2013).

[39] J. Rameau, S. Freutel, A. Kemper, M. A. Sentef, J. Freericks, I. Avigo, M. Ligges, L. Rettig, Y. Yoshida, H. Eisaki *et al.*, Nat. Commun. **7**, 13761 (2016).

[40] J. Reimann, S. Schlauderer, C. Schmid, F. Langer, S. Baierl, K. Kokh, O. Tereshchenko, A. Kimura, C. Lange, J. Güdde *et al.*, Nature (London) **562**, 396 (2018).

[41] A. Eskandari-asl and A. Avella, arXiv:2404.10768.

[42] N. Smith and M. Traum, Phys. Rev. B **11**, 2087 (1975).

[43] F. J. Himpsel and D. E. Eastman, Phys. Rev. B **18**, 5236 (1978).

[44] A. P. Kampf and J. R. Schrieffer, Phys. Rev. B **42**, 7967 (1990).

[45] K. E. Smith and S. D. Kevan, Prog. Solid State Chem. **21**, 49 (1991).

[46] A. Damascelli, Z. Hussain, and Z.-X. Shen, Rev. Mod. Phys. **75**, 473 (2003).

[47] S. Hüfner, *Photoelectron Spectroscopy: Principles and Applications* (Springer Science & Business Media, Cham, 2013)

[48] J. A. Sobota, Y. He, and Z.-X. Shen, Rev. Mod. Phys. **93**, 025006 (2021).

[49] U. Bovensiepen and P. S. Kirchmann, Laser Photon. Rev. **6**, 589 (2012).

[50] C. L. Smallwood, R. A. Kaindl, and A. Lanzara, Europhys. Lett. **115**, 27001 (2016).

[51] X. Zhou, S. He, G. Liu, L. Zhao, L. Yu, and W. Zhang, Rep. Prog. Phys. **81**, 062101 (2018).

[52] F. Boschini, M. Zonno, and A. Damascelli, Rev. Mod. Phys. **96**, 015003 (2024).

[53] M. Weinelt, J. Phys.: Condens. Matter **14**, R1099 (2002).

[54] P. M. Echenique, R. Berndt, E. V. Chulkov, T. Fauster, A. Goldmann, and U. Höfer, Surf. Sci. Rep. **52**, 219 (2004).

[55] J. A. Sobota, S.-L. Yang, A. F. Kemper, J. J. Lee, F. T. Schmitt, W. Li, R. G. Moore, J. G. Analytis, I. R. Fisher, P. S. Kirchmann, T. P. Devereaux, and Z.-X. Shen, Phys. Rev. Lett. **111**, 136802 (2013).

[56] L. Broers and L. Mathey, Phys. Rev. Res. **4**, 013057 (2022).

[57] I. Avigo, R. Cortés, L. Rettig, S. Thirupathaiah, H. S. Jeevan, P. Gegenwart, T. Wolf, M. Ligges, M. Wolf, J. Fink *et al.*, J. Phys.: Condens. Matter **25**, 094003 (2013).

[58] S.-L. Yang, J. A. Sobota, D. Leuenberger, Y. He, M. Hashimoto, D. H. Lu, H. Eisaki, P. S. Kirchmann, and Z.-X. Shen, Phys. Rev. Lett. **114**, 247001 (2015).
[59] U. De Giovannini, G. Brunetto, A. Castro, J. Walkenhorst, and A. Rubio, ChemPhysChem **14**, 1298 (2013).
[60] U. De Giovannini, H. Hubener, and A. Rubio, Nano Lett. **16**, 7993 (2016).
[61] P. Wopperer, U. De Giovannini, and A. Rubio, Eur. Phys. J. B **90**, 51 (2017).
[62] U. De Giovannini, H. Hübener, and A. Rubio, J. Chem. Theory Comput. **13**, 265 (2017).
[63] C. D. Pemmaraju, F. D. Vila, J. J. Kas, S. A. Sato, J. J. Rehr, K. Yabana, and D. Prendergast, Comput. Phys. Commun. **226**, 30 (2018).
[64] N. Tancogne-Dejean and A. Rubio, Sci. Adv. **4**, eaao5207 (2018).
[65] U. De Giovannini, A. Castro *et al.*, Attosecond Molecular Dynamics **13**, 424 (2018).
[66] G. S. Armstrong, M. A. Khokhlova, M. Labeye, A. S. Maxwell, E. Pisanty, and M. Ruberti, Eur. Phys. J. D **75**, 209 (2021).
[67] M. Schüler, J. A. Marks, Y. Murakami, C. Jia, and T. P. Devereaux, Phys. Rev. B **103**, 155409 (2021).
[68] J. K. Freericks, V. M. Turkowski, and V. Zlatić, Phys. Rev. Lett. **97**, 266408 (2006).
[69] D. Golež, L. Boehnke, M. Eckstein, and P. Werner, Phys. Rev. B **100**, 041111(R) (2019).
[70] M. Eckstein, J. Electron Spectrosc. Relat. Phenom. **253**, 147108 (2021).
[71] L. J. DÓnofrio, A. Eskandari-asl, and A. Avella, J. Magn. Magn. Mater. **546**, 168785 (2022).
[72] S. A. Sato, M. Lucchini, M. Volkov, F. Schlaepfer, L. Gallmann, U. Keller, and A. Rubio, Phys. Rev. B **98**, 035202 (2018).
[73] F. Mancini and A. Avella, Adv. Phys. **53**, 537 (2004).
[74] A. Avella and F. Mancini, Phys. Rev. B **75**, 134518 (2007).
[75] A. Avella and F. Mancini, The composite operator method (com), in *Strongly Correlated Systems: Theoretical Methods*, edited by A. Avella and F. Mancini (Springer, Berlin, 2012), pp. 103–141.
[76] A. Avella, Eur. Phys. J. B **87**, 45 (2014).
[77] A. Avella, Adv. Condens. Matter Phys. **2014**, 515698 (2014).
[78] A. Di Ciolo and A. Avella, Condens. Matter Phys. **21**, 33701 (2018).
[79] A. Eskandari-asl and A. Avella, in *Advances in Ultrafast Condensed Phase Physics IV* (SPIE, Seattle, WA, 2024), Vol. 12992, pp. 65–68.
[80] A. A. Mostofi, J. R. Yates, G. Pizzi, Y.-S. Lee, I. Souza, D. Vanderbilt, and N. Marzari, Comput. Phys. Commun. **185**, 2309 (2014).
[81] R. Peierls, Z. Physik **80**, 763 (1933).
[82] S. Ismail-Beigi, E. K. Chang, and S. G. Louie, Phys. Rev. Lett. **87**, 087402 (2001).
[83] L. Yue and M. B. Gaarde, J. Opt. Soc. Am. B **39**, 535 (2022).
[84] J. K. Freericks, H. R. Krishnamurthy, and T. Pruschke, Phys. Rev. Lett. **102**, 136401 (2009).
[85] M. Sentef, A. F. Kemper, B. Moritz, J. K. Freericks, Z.-X. Shen, and T. P. Devereaux, Phys. Rev. X **3**, 041033 (2013).
[86] J. Freericks, H. Krishnamurthy, M. Sentef, and T. Devereaux, Phys. Scr. **T165**, 014012 (2015).
[87] M. Schüler and M. A. Sentef, J. Electron Spectrosc. Relat. Phenom. **253**, 147121 (2021).